Dynamics, emergent statistics, and the mean-pilot-wave potential of walking droplets

Matthew Durey, Paul A. Milewski, and John W. M. Bush

Dynamics, emergent statistics, and the mean-pilot-wave potential of walking droplets

Matthew Durey,[1] Paul A. Milewski,[1] and John W. M. Bush[2]
[1]*Department of Mathematical Sciences, University of Bath, Bath BA2 7AY, United Kingdom*
[2]*Department of Mathematics, Massachusetts Institute of Technology, Cambridge, Massachusetts 02139, USA*

A millimetric droplet may bounce and self-propel on the surface of a vertically vibrating bath, where its horizontal "walking" motion is induced by repeated impacts with its accompanying Faraday wave field. For ergodic long-time dynamics, we derive the relationship between the droplet's stationary statistical distribution and its mean wave field in a very general setting. We then focus on the case of a droplet subjected to a harmonic potential with its motion confined to a line. By analyzing the system's periodic states, we reveal a number of dynamical regimes, including those characterized by stationary bouncing droplets trapped by the harmonic potential, periodic quantized oscillations, chaotic motion and wavelike statistics, and periodic wave-trapped droplet motion that may persist even in the absence of a central force. We demonstrate that as the vibrational forcing is increased progressively, the periodic oscillations become chaotic via the Ruelle-Takens-Newhouse route. We rationalize the role of the local pilot-wave structure on the resulting droplet motion, which is akin to a random walk. We characterize the emergence of wavelike statistics influenced by the effective potential that is induced by the mean Faraday wave field. © 2018 Author(s). All article content, except where otherwise noted, is licensed under a Creative Commons Attribution (CC BY) license (*http://creativecommons.org/licenses/by/4.0/*). https://doi.org/10.1063/1.5030639

A droplet may walk on the surface of a vertically vibrating fluid bath, propelled by the waves generated from all previous impacts. This hydrodynamic pilot-wave system exhibits many features that were previously thought to be exclusive to the quantum realm, such as tunneling, emergent statistics, and quantized droplet dynamics. We herein derive the relationship between the droplet's statistical distribution and the accompanying mean pilot-wave in a very general setting. When the droplet is subject to a central force with its motion confined to a line, we rationalize a number of regimes, including periodic quantized oscillations, chaotic motion, and the emergence of wavelike statistics. In particular, we demonstrate that the mean-pilot-wave potential has a controlling influence on the droplet's dynamics at high vibrational forcing, where the resultant droplet motion is similar to a random walk.

I. INTRODUCTION

A millimetric droplet may bounce on the surface of a vertically vibrating bath of the same fluid; the thin air layer separating the droplet from the bath during impact prevents coalescence.[1,2] Each impact excites a field of temporally decaying Faraday waves, whose longevity depends on the reduced acceleration $\Gamma = A\omega_0^2/g$, where A is the shaking amplitude, $\omega_0/(2\pi)$ is the frequency, and g is the gravitational acceleration. As Γ increases, the bouncing may destabilize to horizontal "walking" across the bath, whereby the droplet is propelled at each impact by the slope of its associated Faraday wave field[3] [see Fig. 1(a)]. The decay time of the Faraday waves increases with Γ for $\Gamma < \Gamma_F$, where the Faraday threshold Γ_F is the critical vibrational acceleration at which Faraday

waves arise in the absence of a droplet. This decay time results in a "path-memory" of previous impacts, where the memory timescale is inversely proportional to the proximity of the Faraday threshold Γ_F.[4] The resulting dynamics are similar in many respects to the pilot-wave dynamics envisaged by de Broglie as a physical framework for understanding quantum mechanics.[5]

The pilot-wave dynamics of this hydrodynamic system gives rise to quantumlike features in a number of settings, and so has prompted the investigation of several hydrodynamic quantum analogs.[6–10] The Faraday wavelength λ_F plays a fundamental role in all of the hydrodynamic quantum analogs, imposing a lengthscale on the interaction between droplets, yielding a discrete set of quantized states for orbiting pairs,[3,11–15] promenading pairs,[15–17] and multi-droplet strings.[18] When a walker is confined to a corral, a wavelike statistical pattern emerges.[19,20] A recent study has shown that the statistical wave form is similar to the time-averaged pilot-wave,[21] but a quantitative relationship between the two was not found. Deducing such a relationship represents one of the key contributions of our study.

Further quantum analogies arise when the droplet is subject to either a central or a Coriolis force, where the latter is realized experimentally in a rotating bath. In both cases, the Faraday wavelength imposes a radial quantization of circular orbits at high wave memory,[22–24] whose stability have been analyzed theoretically.[15,25,26] As the circular orbits destabilize, a new family of stable exotic orbits emerges, revealing a range of extremely rich dynamics.[24,27] In particular, the orbits obtained under a central force exhibit a double quantization in their mean radius and angular momentum, yielding a remarkable analogy to quantum mechanics. The radial quantization

may be rationalized in terms of the energy minimization of the mean Faraday wave field, whose form is determined by the orbital symmetry of each eigenstate.[24] In the chaotic regime arising at high vibrational forcing, a complicated switching process arises between the system's underlying orbital states.[28] Statistical techniques have demonstrated that the double quantization is still present in the droplet's chaotic dynamics.[15,29]

The tendency of the walker system to self-organize into quantized dynamical states was demonstrated by Perrard *et al.*[24,28] and Labousse *et al.*[30] The conceptual value of decomposing the instantaneous pilot-wave field into its mean and fluctuating components was further stressed by Labousse.[31] The merit of this decomposition in connecting the dynamics and statistics of pilot-wave systems is demonstrated here through consideration of a relatively simple geometry.

The complex structure of the exotic (non-circular) orbits has to date prohibited a comprehensive theoretical investigation of their dynamics in the periodic and chaotic regimes. Such a study is likely to shed new light on the quantumlike behavior and the role of the mean wave field in the long path-memory limit. To develop the techniques required for such an analysis, we focus this work on the dynamics in a harmonic potential where the droplet motion is restricted to a line and accompanied by a two-dimensional wave field [Fig. 1(a)]. This system exhibits extremely rich dynamics and analogies to quantum mechanics, whilst remaining simple enough to form the basis of a theoretical investigation that provides a foundational mathematical framework for future studies of more geometrically complex systems.

In the classical harmonic oscillator $mx''(t) + \kappa x(t) = 0$ with spring constant κ, a particle of mass m enters into simple harmonic motion with fixed frequency $\omega = \sqrt{\kappa/m}$. The energy of the particle varies continuously with the initial conditions, and the motion is entirely deterministic. Conversely, in quantum mechanics, the particle energy E is quantized with $E_n = \hbar\omega(n + 1/2)$ (where $\hbar$ is the reduced Planck's constant and $n \in \mathbb{N}$), where for each energy level there is an associated probability distribution for the particle's position. In what follows, we will demonstrate that the dynamics of the hydrodynamic pilot-wave system vary from classical to quantumlike, depending on the relative magnitudes of the wave and central forces. At low wave amplitude, the balance of wave and drag forces yields a stable limit cycle, whose oscillation amplitude and period vary continuously

with the spring constant. When the waves dominate, the surviving pilot-wave from previous crossings of the bath causes significant variations in the droplet velocity, yielding quantized droplet range and wavelike statistics for the droplet position. The quantization length is $\lambda_F/2$, and our study reveals that the Faraday wavelength also plays a pivotal role in the chaotic dynamics emerging near the Faraday threshold.

We herein apply the model of Durey and Milewski[15] to elucidate the emergent quantizations, wavelike statistics, and the role of the mean wave field in the system's periodic and chaotic dynamics. In Sec. II B, we prove that the droplet's stationary probability distribution is related to the mean pilot-wave field via a convolution with the wave field of a bouncing droplet. In Sec. III, we extend the methods of earlier work to analyse the amplitude and stability of periodic oscillations, where we see the onset of quantization and wavelike statistics. In the limit of $\Gamma \to \Gamma_F$, periodic wave-trapped solutions arise in which the droplet's oscillatory motion persists even in the absence of an external force ($\kappa = 0$) and the mean wave field acts as an effective potential (Sec. III C). In Sec. IV A, we demonstrate that this system exhibits the Ruelle-Takens-Newhouse route to chaos.[32,33] At extremely high memory (as considered in Sec. IV B), the wave field dominates the droplet dynamics, yielding a short-timescale droplet motion similar to a random walk, and a long-timescale behavior influenced by an effective potential prescribed by the mean wave field. By detrending the long-timescale behavior induced by slow variations in the Faraday wave field, we see the emergence of pronounced wavelike statistics whose peaks are determined by the random walk dynamics.

II. DISCRETE-TIME MODEL

The dynamics of this system are depicted by the schematic diagram in Fig. 1(b). We assume that the droplet and bath are in periodic subharmonic resonance (as observed in experiments over a broad parameter regime[34]), and we model the impacts as instantaneous and localized at a point. This approximation is reasonable for describing short impacts with a small droplet, which we model as a rigid sphere. A full derivation of this model can be found in Ref. 15.

The semi-infinite fluid bath is governed by linear quasi-potential flow, which includes weak dissipative effects at high Reynolds number.[35–37] The harmonic velocity potential ϕ and wave perturbation η couple with the prescribed impact
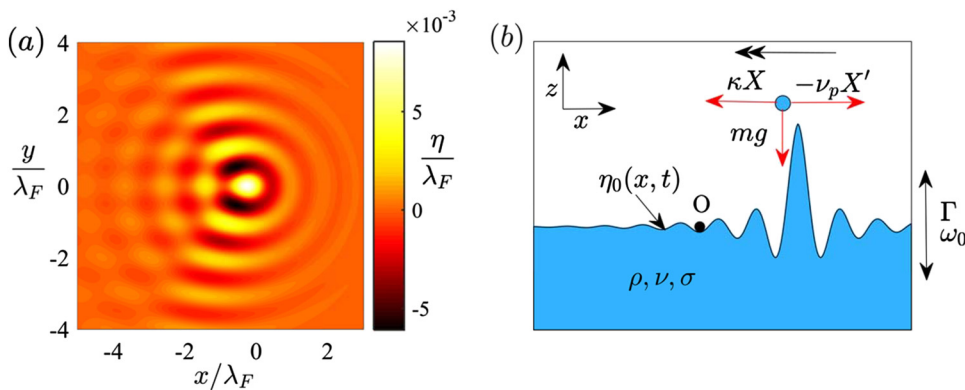

FIG. 1. (a) The wave field $\eta(\mathbf{x}, t)$ of a steady walking droplet at impact [in the absence of a central force ($\kappa = 0$)], as computed by Durey and Milewski[15] for $\Gamma/\Gamma_F = 0.97$. The droplet is located at the origin and walks to the right along the line $y = 0$, where $\mathbf{x} = (x, y)$. (b) Two-dimensional schematic diagram of the fluid system with free surface $\eta_0 \equiv \eta|_{y=0}$. The forces acting on the droplet are denoted by red arrows, including the central force $\kappa \mathbf{X}(t)$ that acts towards the origin O. The system parameters considered in our simulations and analysis are given in Table I.

pressure $P_D(\boldsymbol{x},t) = f(t)\delta[\boldsymbol{x} - \boldsymbol{X}(t)]$, where $\boldsymbol{x} = (x,y)$ is the position on the fluid surface and $\boldsymbol{X}(t)$ is the horizontal droplet position. For instantaneous impacts with subharmonic vertical motion, we require $f(t) = mg\sum_{n=0}^{\infty}\delta(t/T - n)$, where $T = 4\pi/\omega_0$ is the Faraday period and m is the droplet mass.[38] The vibrating frame of reference introduces the effective gravity $g_\Gamma(t) = g[1 - \Gamma\cos(\omega_0 t + \beta)]$, where β denotes the droplet's impact phase.

Following the model of Moláček and Bush,[38] the horizontal droplet position is governed by

$$m\boldsymbol{X}''(t) + \nu_p\boldsymbol{X}'(t) + \kappa\boldsymbol{X}(t)$$
$$= -f(t)\{\nabla\eta[\boldsymbol{X}(t),t] + c\sqrt{\rho R_0/\sigma}\,\boldsymbol{X}'(t)\}, \qquad (1)$$

with parameters given in Table I. During flight ($f = 0$), inertia is balanced by the horizontal central force and Stokes' drag with coefficient $\nu_p = 6\pi R_0\mu_{air}$. During impact ($f > 0$), the reaction force imparts a (linearized) kick to the droplet, which is countered by skidding friction characterized by the dimensionless drag coefficient $c > 0$,[38] whose value is discussed below.

A. Dimensionless variables

Henceforth, we describe the dynamics in terms of dimensionless variables, where we scale lengths with the Faraday wavelength $\lambda_F = 0.51$ cm, time t with the subharmonic bouncing period $T = 4\pi/\omega_0$, force f with $f_0 = mg$, and pressure P_D with $P_0 = f_0/\lambda_F^2$. This yields the following dimensionless parameters:

$$\epsilon = \frac{\nu T}{\lambda_F^2}, \quad B = \frac{\sigma T^2}{\rho\lambda_F^3}, \quad G = \frac{gT^2}{\lambda_F}, \quad M = \frac{m}{\rho\lambda_F^3},$$
$$R = \frac{R_0}{\lambda_F}, \quad \tilde{\nu}_p = \frac{\nu_p T}{m}, \quad \tilde{\kappa} = \frac{\kappa T^2}{m}.$$

Typical parameter values from Table I give reciprocal Reynolds number $\epsilon \approx 0.019$, Bond number $B \approx 0.102$, $G \approx 1.201$, $M \approx 0.0017$, $R \approx 0.075$, $\tilde{\nu}_p \approx 0.01$, and vibration number $\Omega \equiv 4\pi\sqrt{R^3/B} = 0.8$.[39] The dimensionless potential strength $\tilde{\kappa} \geq 0$ is a free parameter of both the model and experiments, with $10^{-3} \lesssim \tilde{\kappa} \lesssim 10^{-1}$. The dynamics are largely insensitive to changes in the skidding friction c and impact phase β; thus, we fix $c = 0.33$ and $\beta = \pi$.[15]

To reduce the fluid system from partial to ordinary differential equations, we spectrally decompose ϕ and η in the horizontal plane. The simple "Dirichlet-to-Neumann" map for

TABLE I. Fluid and droplet parameters used in this model.

Variable	Value	Description
σ	2.06×10^{-2} kg s^{-2}	Surface tension
ρ	949 kg m^{-3}	Fluid density
ν	2×10^{-5} m^2 s^{-1}	Kinematic viscosity (fluid)
μ_{air}	1.8×10^{-5} kg m^{-1} s^{-1}	Dynamic viscosity (air)
g	9.8 m s^{-2}	Gravity
ω_0	$80 \times 2\pi$ s^{-1}	Vibration frequency ($\times 2\pi$)
R_0	3.8×10^{-4} m	Droplet radius
m	2.2×10^{-7} kg	Droplet mass
ν_p	1.3×10^{-7} kg s^{-1}	Stokes' drag coefficient

ϕ under this decomposition allows us to eliminate ϕ in favour of η, which we express as

$$\eta(\boldsymbol{x},t) = \sum_{m=-\infty}^{\infty}\int_0^{\infty}ka_m(t;k)\Phi_m(\boldsymbol{x};k)\,dk, \qquad (2)$$

with orthogonal basis functions $\Phi_m(\boldsymbol{x};k) \equiv J_m(kr)e^{im\theta}$, where $\boldsymbol{x} = (r,\theta)$ in polar coordinates and i is the imaginary unit. As η is real and $J_m(z) = (-1)^m J_{-m}(z)$ for all $m \in \mathbb{Z}$, the complex coefficients a_m satisfy the reality condition $a_{-m} = (-1)^m a_m^*$ for all m, where $*$ denotes the complex conjugate. This basis decomposition yields a system of inhomogeneous damped Mathieu equations for the wave amplitudes a_m, where the inhomogeneity arises from the instantaneous forcing at impact. Assuming $\boldsymbol{X}(t)$ and $\eta(\cdot,t)$ are continuous across impacts, we obtain nonlinear jumps in $\boldsymbol{X}'$ and η_t at impact times $t = t_n \equiv n$, which appear in (6) and (7) below.

During flight ($t \neq t_n$), the wave and droplet dynamics decouple and evolve according to

$$(\partial_t + \gamma_k)^2 a_m + [\omega_k^2 - \Gamma\omega_{g,k}^2\cos(4\pi t + \beta)]a_m = 0, \qquad (3)$$

$$\boldsymbol{X}''(t) + \tilde{\nu}_p\boldsymbol{X}'(t) + \tilde{\kappa}\boldsymbol{X}(t) = 0, \qquad (4)$$

where $\gamma_k \equiv 2\epsilon k^2$, $\omega_k^2 \equiv Gk + Bk^3$, and $\omega_{g,k}^2 \equiv Gk$. As (3) is of Floquet form with period $1/2$, we evolve the system between impacts ($t_{n-1}^+ \mapsto t_n^-$) using principal fundamental matrices $\boldsymbol{M}_k(\Gamma) \in \mathbb{R}^{2\times2}$ for the wave amplitudes [Eq. (3)] and $\boldsymbol{F}(\tilde{\kappa}) \in \mathbb{R}^{4\times4}$ for the droplet dynamics (4). This yields the 3-stage map from $t_{n-1}^+ \mapsto t_n^+$:

1. Compute the next droplet position and the pre-impact velocity

$$\begin{pmatrix}\boldsymbol{X}(t_n) \\ \boldsymbol{X}'(t_n^-)\end{pmatrix} = \boldsymbol{F}(\tilde{\kappa})\begin{pmatrix}\boldsymbol{X}(t_{n-1}) \\ \boldsymbol{X}'(t_{n-1}^+)\end{pmatrix}. \qquad (5)$$

2. Update the wave amplitudes $\forall k > 0$ and $\forall m \in \mathbb{Z}$

$$\begin{pmatrix}a_m(t_n;k) \\ a_m'(t_n^+;k)\end{pmatrix} = \boldsymbol{M}_k(\Gamma)\begin{pmatrix}a_m(t_{n-1};k) \\ a_m'(t_{n-1}^+;k)\end{pmatrix}$$
$$- p_k\Phi_m^*[\boldsymbol{X}(t_n);k]\begin{pmatrix}0 \\ 1\end{pmatrix}. \qquad (6)$$

3. Apply the droplet jump conditions

$$\boldsymbol{X}'(t_n^+) = (1 - F)\boldsymbol{X}'(t_n^-) - H\nabla\eta[\boldsymbol{X}(t_n),t_n], \qquad (7)$$

where $F = 1 - \exp(-cG\sqrt{R/B})$, $H = (F/c)\sqrt{B/R}$, and $p_k = kMG/(2\pi)$. Equations (6) and (7) couple through $\nabla\eta$ given by (2).

The wave "memory" M_e is defined as the timescale over which the Faraday waves decay, which is a proxy for the number of past impacts that influence the current dynamics.[4] This appears naturally from the eigenvalues of $\boldsymbol{M}_k(\Gamma)$, which we write as $\exp(-s_1)$ and $\exp(-s_2)$ for $s_i = s_i(k,\Gamma) \in \mathbb{C}$, where $0 \leq \text{Re}(s_1) \leq \text{Re}(s_2)$. The dominant exponent $s_1(k,\Gamma)$ is real and positive in a neighborhood of (k_F, Γ_F), with $s_1(k_F, \Gamma_F) = 0$. For $\Gamma < \Gamma_F$, we thus define

$$M_e(\Gamma) = \max_k\{s_1(k,\Gamma)^{-1}|s_1 \in \mathbb{R}\} \sim \frac{T_d(\Gamma)}{1 - \Gamma/\Gamma_F} \qquad (8)$$

as $\Gamma \to \Gamma_F$, where $T_d(\Gamma) \sim 0.6$.[15,36] While this parameter diverges as $\Gamma \to \Gamma_F$, we note that the description of the wave
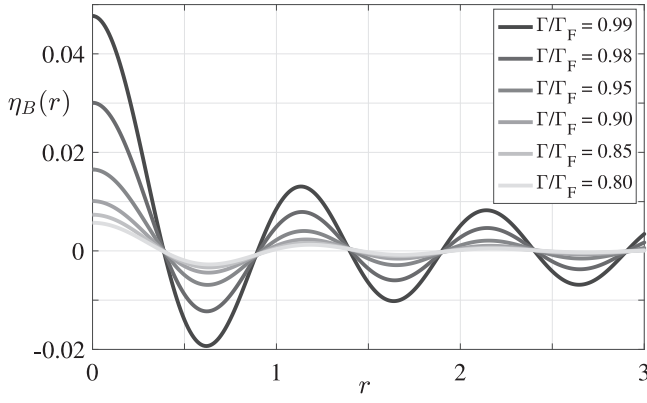
FIG. 2. The axisymmetric wave field of a bouncer $\eta_B(r)$ at impact for different values of $\Gamma < \Gamma_F$ (where $r = |\boldsymbol{x}|$). All lengths are non-dimensionalized by λ_F.

field in terms of linear Faraday waves also breaks down in this limit, where nonlinear effects are expected to become significant.

To implement the model given by Eqs. (5)–(7), we make an appropriate discretisation of the wavenumbers k and truncate the Bessel modes m, as detailed in Ref. 15. The diagonal structure in k and m allows for simulations at typically 1000 impacts per second[40] (this is 25 times faster than the experimental timescale). By using the methods developed in Sec. III, the discrete-time formulation (5)–(7) also allows for efficient computation of the system's periodic states with linear stability analysis.

B. Long-time statistical behavior

Previous investigations into the long-time dynamics of this hydrodynamic pilot-wave system have focused primarily on the statistical distribution of the droplet position $\mu(\boldsymbol{x})$, rather than considering the mean pilot-wave $\bar{\eta}(\boldsymbol{x})$ at impact, as defined by

$$\bar{\eta}(\boldsymbol{x}) = \lim_{N \to \infty} \frac{1}{N} \sum_{n=1}^{N} \eta(\boldsymbol{x}, t_n). \qquad (9)$$

A recent study of walker motion in corrals pointed out that the two take a similar form;[21] however, a quantitative relation between the two was not deduced. We proceed by proving that (in an unbounded domain) these two quantities are in fact related via the convolution $\bar{\eta} = \eta_B * \mu$. Here, $\eta_B(\boldsymbol{x})$ is the axisymmetric wave field of a stationary bouncing droplet at impact, which is the wave field generated by infinitely many periodic impacts at $\boldsymbol{x} = \boldsymbol{0}$ for a given $\Gamma < \Gamma_F$ (see Fig. 2). We note that although we focus on the dynamics in the walking regime (in which the bouncing state is unstable), the associated bouncer wave field η_B still plays a pivotal role in the long-time statistics.

The physical intuition behind this convolution result is as follows. For stationary dynamics, each point $\boldsymbol{x}$ in the domain (within the support of μ) is visited infinitely many times. If all points were visited equally, each would thus contribute equally to the mean wave field, in the amount of $\eta_B(\boldsymbol{x})$. Since they are not visited equally, the contribution of each point

$\eta_B(\boldsymbol{x})$ must be weighted by $\mu(\boldsymbol{x})$. Our result not only combines three key quantities of this pilot-wave system but is also valid for periodic motion and ergodic dynamics, such as in the chaotic regime. As will be seen, this convolution result is particularly useful for elucidating the dynamics at high memory, including periodic wave-trapped behavior (Sec. III C) and chaotic dynamics near the Faraday threshold (Sec. IV C).

Theorem 1. *Assuming there exists a stationary probability distribution $\mu(\boldsymbol{x})$ for the droplet position and that the system dynamics are ergodic, then the mean wave field $\bar{\eta}(\boldsymbol{x})$ [as defined by Eq. (9)] satisfies*

$$\bar{\eta}(\boldsymbol{x}) = \int_{\mathbb{R}^2} \eta_B(\boldsymbol{x} - \boldsymbol{y}) \mu(\boldsymbol{y}) \, \mathrm{d}\boldsymbol{y} = (\eta_B * \mu)(\boldsymbol{x}), \qquad (10)$$

where $\eta_B(\boldsymbol{x})$ is the radially symmetric wave field of a bouncer centred at the origin.

Proof. We define $\boldsymbol{a}_m^n(k) \equiv [a_m(t_n; k), a_m'(t_n^+; k)]^T$ and rewrite (6) as

$$\boldsymbol{a}_m^n(k) = \boldsymbol{M}_k \boldsymbol{a}_m^{n-1}(k) - p_k \Phi_m^*[\boldsymbol{X}(t_n); k] \boldsymbol{e}_2, \qquad (11)$$

where $\boldsymbol{e}_j$ is the jth basis vector. We then define $\bar{\boldsymbol{a}}_m(k) \equiv \lim_{N \to \infty} \frac{1}{N} \sum_{n=1}^{N} \boldsymbol{a}_m^n(k)$ to be the wave amplitudes corresponding to the mean wave field $\bar{\eta}$. By taking the mean of (11) over N impacts and considering the limit $N \to \infty$, the ergodic theorem allows for the replacement of time averages in the last term with spatial averages, giving

$$\bar{\boldsymbol{a}}_m(k) = \boldsymbol{M}_k \bar{\boldsymbol{a}}_m(k) - p_k \boldsymbol{e}_2 \int_{\mathbb{R}^2} \Phi_m^*(\boldsymbol{y}; k) \mu(\boldsymbol{y}) \, \mathrm{d}\boldsymbol{y}.$$

For $\Gamma < \Gamma_F$, the matrix $(\boldsymbol{I} - \boldsymbol{M}_k)$ is nonsingular, so we may solve for $\bar{\boldsymbol{a}}_m(k)$ for all m and k.

By defining $a_B(k; \Gamma) = -p_k \boldsymbol{e}_1^T [\boldsymbol{I} - \boldsymbol{M}_k(\Gamma)]^{-1} \boldsymbol{e}_2$ and

$$f_m(k) = \int_{\mathbb{R}^2} \Phi_m^*(\boldsymbol{y}; k) \mu(\boldsymbol{y}) \, \mathrm{d}\boldsymbol{y},$$

we have

$$\bar{\eta}(\boldsymbol{x}) = \sum_{m=-\infty}^{\infty} \int_0^{\infty} k a_B(k; \Gamma) \Phi_m(\boldsymbol{x}; k) f_m(k) \, \mathrm{d}k$$

$$= \int_{\mathbb{R}^2} \mu(\boldsymbol{y}) \int_0^{\infty} k a_B(k; \Gamma) J_0(k|\boldsymbol{x} - \boldsymbol{y}|) \, \mathrm{d}k \, \mathrm{d}\boldsymbol{y},$$

where we have used Graf's addition theorem[41] to write

$$J_0(k|\boldsymbol{x} - \boldsymbol{y}|) = \sum_{m=-\infty}^{\infty} \Phi_m(\boldsymbol{x}; k) \Phi_m^*(\boldsymbol{y}; k).$$

The result (10) follows since the wave field of a bouncer centred at the origin for given Γ is $\eta_B(\boldsymbol{x}) = \int_0^{\infty} k a_B(k; \Gamma) J_0(k|\boldsymbol{x}|) \, \mathrm{d}k$.[15] $\qquad \square$

We have proved similar convolution results for the models of Fort et al.,[22] and Oza et al.,[42] where different modeling assumptions were made on the wave field dynamics and the droplet-wave coupling. In fact, we generalize the convolution relationship (10) to a wider pilot-wave framework in Appendix A, which includes the pilot-wave dynamics in a confined geometry. In this more general case, the integral kernel η_B is replaced by a function that no longer exhibits translational invariance.

The result in Theorem 1 rests on the assumptions that a stationary distribution exists and that the pilot-wave dynamics are ergodic. It has been observed experimentally that when the droplet's motion is confined (by a harmonic potential[24] or the boundary walls of a corral[19,21]), a stationary distribution may emerge. The ergodicity assumption is more delicate. It has been observed in the one-dimensional tunneling pilot-wave model of Nachbin *et al.*[8] that several chaotic trajectories with different initial conditions had the same statistical properties as a single longer run, suggesting that the process is indeed ergodic in that particular configuration. We note, however, that when multiple stable states exist (such as in the case of hysteresis), the long-time behavior may depend on the initialisation of the pilot-wave system, rendering the ergodicity assumption invalid.

To overcome this difficulty, we prove an analogous result to Theorem 1 valid when the pilot-wave dynamics are periodic for all time, namely, $X(t_{n+Q}) = X(t_n)$ for all n and some finite $Q \in \mathbb{N}$. This corollary does not require any assumptions about the existence or uniqueness of a stationary distribution, nor does it require the ergodic hypothesis.

Corollary 1. *If there exists $Q \in \mathbb{N}$ such that $X(t_{n+Q}) = X(t_n)$ for all n, then the mean wave field $\bar{\eta}(\mathbf{x}) = Q^{-1} \sum_{n=1}^{Q} \eta(\mathbf{x}, t_n)$ satisfies*

$$\bar{\eta}(\mathbf{x}) = \int_{\mathbb{R}^2} \eta_B(\mathbf{x} - \mathbf{y}) \mu(\mathbf{y}) \, \mathrm{d}\mathbf{y} = (\eta_B * \mu)(\mathbf{x}),$$

where $\eta_B(\mathbf{x})$ is the radially symmetric wave field of a bouncer centred at the origin and $\mu(\mathbf{x}) = Q^{-1} \sum_{n=1}^{Q} \delta[\mathbf{x} - X(t_n)]$.

Proof. Using the definition of $\mathbf{a}_m^n(k)$ from the proof of Theorem 1, we take the sum $\sum_{n=1}^{Q}$ of both sides of Eq. (11), giving

$$\sum_{n=1}^{Q} \mathbf{a}_m^n(k) = \mathbf{M}_k \sum_{n=1}^{Q} \mathbf{a}_m^{n-1}(k) - p_k \mathbf{e}_2 \sum_{n=1}^{Q} \Phi_m^*[X(t_n); k].$$

By the assumed periodicity, we observe that $\mathbf{a}_m^0 = \mathbf{a}_m^Q$. Hence, by defining $\bar{\mathbf{a}}_m(k) \equiv Q^{-1} \sum_{n=1}^{Q} \mathbf{a}_m^n(k)$ and $\mu(\mathbf{x}) = Q^{-1} \sum_{n=1}^{Q} \delta[\mathbf{x} - X(t_n)]$, we obtain

$$\bar{\mathbf{a}}_m(k) = \mathbf{M}_k \bar{\mathbf{a}}_m(k) - p_k \mathbf{e}_2 \int_{\mathbb{R}^2} \Phi_m^*(\mathbf{y}; k) \mu(\mathbf{y}) \, \mathrm{d}\mathbf{y}.$$

The conclusion of the proof is identical to that of Theorem 1. □

Henceforth, we consider the case where the droplet motion is confined to a line. For $\mu(\mathbf{x}) = \rho_X(x) \delta(y)$ [where $\mathbf{x} = (x, y)$], Theorem 1 and Corollary 1 both simplify to $\bar{\eta}_0(x) = (\rho_X * \eta_B)(x)$, where $\bar{\eta}_0 \equiv \bar{\eta}|_{y=0}$ is the mean wave field along the x-axis. We demonstrate in Appendix B that in the case where the period $Q \to \infty$, the result to Corollary 1 remains robust, even when the probability distribution $\rho_X(x)$ is approximated by a histogram.

III. PERIODIC SOLUTIONS

We seek periodic solutions to the nonlinear discrete-time map (5)–(7) with motion restricted to the x-axis, so $X(t) \equiv [X(t), 0]$ and $a_m \in \mathbb{R}$ for all m. For notational convenience,

we denote

$$X_n = X(t_n), \quad V_n^\pm = X'(t_n^\pm), \quad \eta_0(x, t) = \eta(x, 0, t),$$

where $G_n = \partial_x \eta_0(X_n, t_n)$ is the wave field gradient along the x-axis at impact n.

For any given $(\Gamma, \tilde{\kappa})$, the frequency of the periodic oscillation is generally incommensurate with the Faraday frequency, which complicates the analysis for our discrete-time system. To resolve this, we exploit continuity of the parameter space to seek a subset of solutions where the oscillation period $\mathcal{P}$ satisfies $\mathcal{P} = \varphi N$ ($N \in \mathbb{N}$ and $\varphi \in \mathbb{Q}$) for a given Γ, and solve for $\tilde{\kappa}$ (it should be noted that in this case, there is a relationship between the oscillation period $\mathcal{P} \in \mathbb{Q}$ and the number of impacts $Q \in \mathbb{N}$ such that $X_n = X_{n+Q}$ for all n). Typically, $\varphi = 2$ is sufficient to resolve the solution curve, which corresponds to the droplet crossing the bath once after N impacts. This case yields reflection conditions (for all $m \in \mathbb{Z}$ and $k > 0$)

$$X_N = -X_0, \tag{12a}$$

$$V_N^+ = -V_0^+, \tag{12b}$$

$$a_m(t_N; k) = (-1)^m a_m(t_0; k), \tag{12c}$$

$$a_m'(t_N^+; k) = (-1)^m a_m'(t_0^+; k). \tag{12d}$$

For given Γ and N, we use a Newton method to compute the periodic states for $(N + 1)$ unknowns $\boldsymbol{\theta} = (X_0, \tilde{\kappa}, G_1, \ldots, G_{N-1})$, with the details given in Appendix C. We exploit continuity of the solution branch by using as an initial guess a converged solution along the same branch. The idea is to use the iterative map (5)–(7) to first obtain droplet positions at each impact and then use the reflection conditions (12c) and (12d) to find the unique corresponding wave field. This gives the gradients at each impact, which need to be consistent with the initial guess, and also the final droplet position and velocity, which need to be consistent with the reflection conditions (12a) and (12b). The stability is analyzed through computing the eigenvalues of the linearized N-fold iterative map for perturbations about the periodic state, where the periodic solution is defined as asymptotically unstable if an eigenvalue lies outside the unit disc in the complex plane.

We characterize the periodic solutions in terms of the period $\mathcal{P}$, amplitude $\mathcal{A}$, and the mean energy of the wave field $\bar{\mathcal{E}} = \mathcal{P}^{-1} \int_0^{\mathcal{P}} \mathcal{E}(t) \, \mathrm{d}t$, where $\mathcal{E}(t)$ is the wave field energy at time t, as defined in Ref. 15. This is the additional energy of the fluid induced by the past droplet impacts, which has components of gravitational potential energy, surface energy, and the kinetic energy contribution from the potential flow within the bath. The energy $\bar{\mathcal{E}}$ also includes the wave field energy during droplet flight, which cannot be captured in models that neglect the oscillatory motion of the wave field between impacts.[22,42] We compare the energy to the mean energy of a bouncing droplet $\bar{\mathcal{E}}_B$ at the given memory, where $\bar{\mathcal{E}} \to \bar{\mathcal{E}}_B$ as $\mathcal{A} \to 0^+$. We also neglect the mean energy contribution from the droplet's horizontal and vertical motions; the former is several magnitudes smaller than the mean wave energy, and the latter is constant in our model due to the imposed periodic vertical motion.[15]

A. From bouncing to oscillating

We first consider the onset of small-amplitude oscillation that arises for a sufficiently weak spring constant. In the limit $\mathcal{A} \to 0$, the degenerate case $\mathcal{P} = 1$ describes a bouncer at the origin for a given Γ, which is stable for $\tilde{\kappa} > \tilde{\kappa}_c(\Gamma)$. Thus, the bouncing state can persist beyond the free-space ($\tilde{\kappa} = 0$) walking threshold; a sufficiently steep harmonic potential may trap the droplet at the origin. For $\tilde{\kappa} < \tilde{\kappa}_c$, the bouncing destabilizes via a supercritical Neimark-Sacker bifurcation, where the period of unstable oscillation $\mathcal{P}^\star > 0$ is given by the argument of the unstable complex conjugate eigenvalues of the stability matrix. A stable limit cycle forms after an initial transient, whose period $\mathcal{P}$ and amplitude $\mathcal{A}$ we compute directly. For sufficiently small oscillations ($\mathcal{A} \lesssim 0.15$), the period associated with the destabilising mode of the bouncer is well approximated by the limit cycle period, with $|\mathcal{P} - \mathcal{P}^\star| \lesssim 1$, as shown in Fig. 3. In the limit $\mathcal{A} \to 0^+$, we have $\mathcal{P} \to \mathcal{P}_c(\Gamma) \in (0, \infty)$; this infinitesimal oscillation amplitude with a finite frequency is analogous to the small radius limit of circular orbits.[25]

B. From classical to quantized dynamics

In Fig. 4, we show the dependence of the oscillation amplitude $\mathcal{A}$ on the spring constant $\tilde{\kappa}$, period $\mathcal{P}$, and wave energy $\bar{\mathcal{E}}$. For weak memory ($\Gamma/\Gamma_F = 0.9$), all oscillations are stable (blue curves) and the amplitude grows monotonically as $\tilde{\kappa}$ decreases. The period increases approximately linearly with the amplitude for large oscillations under a weak central force, which dominates the wave force only at the extrema of the periodic motion.

As the memory is increased ($\Gamma/\Gamma_F = 0.94$), unstable oscillations emerge (red curves), corresponding to forbidden oscillation amplitudes. Strikingly, the unstable oscillations have the largest mean energy $\bar{\mathcal{E}}$, and as more oscillations destabilize for $\Gamma/\Gamma_F = 0.96$, the remaining stable oscillations (blue curves) have the lowest mean wave field energy, suggesting an underlying energy minimization principle. A similar energy minimization was also observed for circular orbits in a harmonic potential and at the bifurcation between bouncing and walking.[15] The remaining stable oscillations exhibit quantization of the oscillation amplitude, with a large number of stable plateaus (blue) in the ($\tilde{\kappa}, \mathcal{A}$)-plane emerging for a fixed memory, as apparent in Fig. 4(c). There are, moreover, several examples of hysteresis [Fig. 4(c)]. The emergent quantization is analogous to that arising in the quantum harmonic oscillator, where the increment between energy levels

$\delta E = \hbar \omega$ is fixed. Similarly, the fluid system exhibits a quantization in the oscillation amplitude $\mathcal{A}$ with fixed increment $\delta \mathcal{A} \approx 1/2$ equal to the radial quantization increment observed for circular orbits.[15,24,26]

In Fig. 5, we plot the computed pilot-wave field $\eta_0(x, t_n)$ and droplet position X_n at impact over two periods of the oscillatory periodic state. When the central force dominates the wave force [Fig. 5(a)], the droplet motion is approximately sinusoidal. In contrast, at larger wave memory [Fig. 5(b)], the pilot-wave has a strong influence on the droplet's oscillatory motion, resulting in a pronounced departure from the sinusoidal behavior.

In Fig. 6, we plot the phase space and corresponding probability distribution for simulation of the stable oscillation states with $\tilde{\kappa} = 0.012$ (corresponding to the black circles in Fig. 4). At the point of maximum range, the droplet reverses, turning over the back of its pilot-wave field, causing a sharp increase in the droplet speed, to approximately twice the free walking speed (see supplementary material). The wave field generated during previous crossings of the bath thus substantially modulates the droplet speed during transit, indicating that the weak-acceleration limit approximation is not valid in this regime.[43,44] As reported for the case of corrals,[19,21] this speed-modulation is responsible for the emergence of wave-like statistics, where the maxima of the stationary probability distribution $\rho_X(x)$ arise when the droplet speed is lowest. Through its modulation of the droplet speed, the wavelength of the pilot-wave thus prescribes the wavelength of the statistical wave, as is most apparent in Fig. 6(c). We see that for all values of Γ/Γ_F, the mean wave field $\bar{\eta}_0(x)$ and probability distribution $\rho_X(x)$ take a similar form on the interval $x \in [-\mathcal{A}, \mathcal{A}]$, as expected on the basis of our convolution relationship $\bar{\eta}_0 = \rho_X * \eta_B$.

For $\Gamma/\Gamma_F = 0.96$, we plot the mean Faraday wave field $\bar{\eta}(\mathbf{x})$ in Fig. 7. Since $\rho_X(x)$ is largest near the oscillation extrema, we see corresponding peaks in $\bar{\eta}$ near the points $(x, y) = (\pm \mathcal{A}, 0)$. Furthermore, we typically see $\bar{\eta}_0(x) > 0$ for all $x \in [-\mathcal{A}, \mathcal{A}]$ since the local wave field is generally maximal near the droplet [for example, see the free-walker wave field in Fig. 1(a)]. Moreover, the symmetry about $x = 0$ of the statistical distribution ensures symmetry in the mean wave field.

C. Wave-trapped solutions

As Γ/Γ_F increases, we observe that the plateaus of stable oscillations in the ($\tilde{\kappa}, \mathcal{A}$)-plane become flatter and wider (see Fig. 4). We thus seek solutions where the periodic motion is
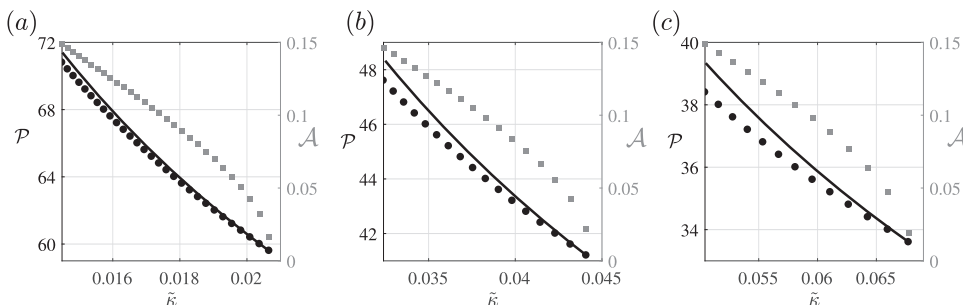

FIG. 3. Small amplitude periodic oscillations for dimensionless period $\mathcal{P}$ (circles) and amplitude $\mathcal{A}$ (squares). The period associated with the destabilising mode of the bouncer $\mathcal{P}^\star$ is given by the black curve. (a) $\Gamma/\Gamma_F = 0.81$, (b) $\Gamma/\Gamma_F = 0.82$, and (c) $\Gamma/\Gamma_F = 0.83$. In the limit $\mathcal{A} \to 0$, the droplet is trapped in a bouncing state that is stabilized by the harmonic potential.
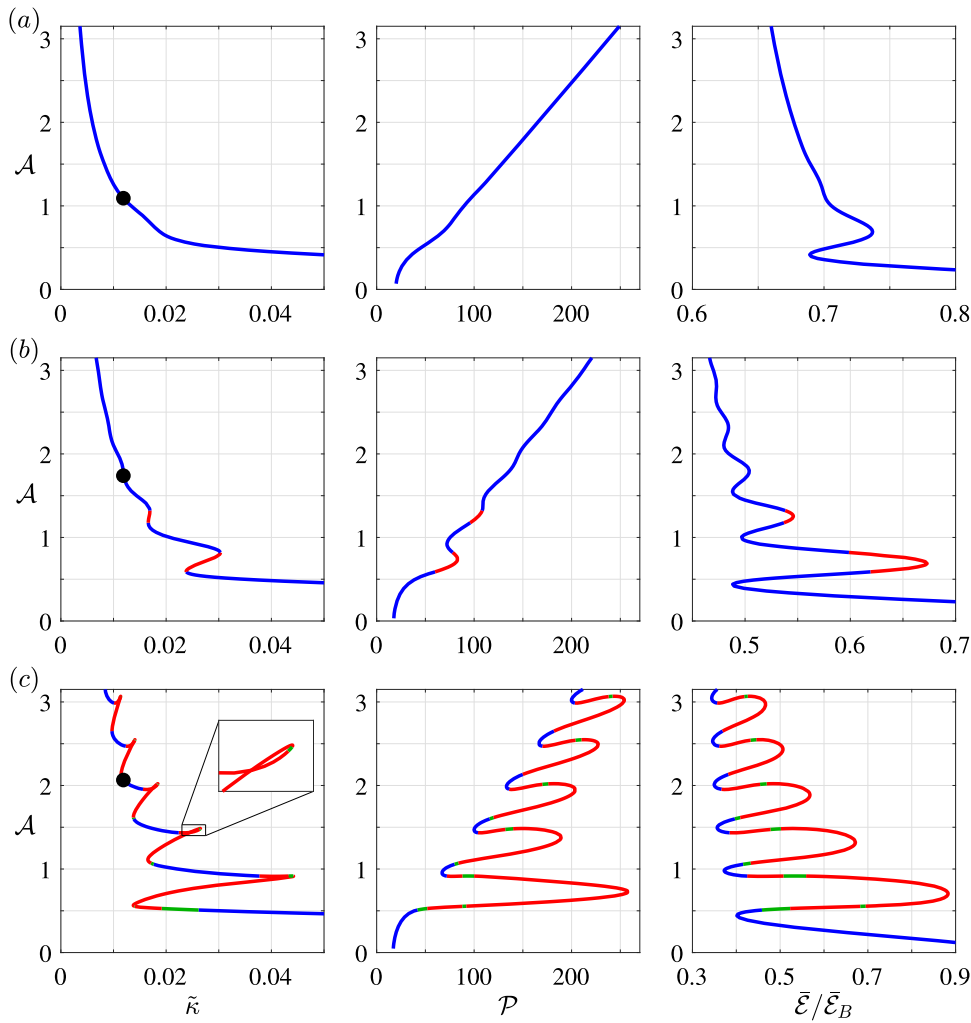
FIG. 4. The emergence of quantization for the periodic states computed in Sec. III. The oscillation amplitude $\mathcal{A}$ is plotted as a function of spring constant $\tilde{\kappa}$ (first column), period $\mathcal{P}$ (second column), and the mean wave field energy relative to that of a bouncer $\bar{\mathcal{E}}/\bar{\mathcal{E}}_B$ (third column). For each row, we have (a) $\Gamma/\Gamma_F = 0.90$, (b) $\Gamma/\Gamma_F = 0.94$, and (c) $\Gamma/\Gamma_F = 0.96$. The curve colors denote stability types (blue: stable, green: unstable with all unstable eigenvalues complex conjugate pairs, red: unstable with at least one real unstable eigenvalue). The black circles at $\tilde{\kappa} = 0.012$ in the $(\tilde{\kappa}, \mathcal{A})$ plots correspond to the simulated oscillation amplitudes in Fig. 6. (c) The inset in the $(\tilde{\kappa}, \mathcal{A})$ plot details the loop structure in the corresponding square.

sustained even in the absence of a harmonic potential ($\tilde{\kappa} = 0$), in which the mean wave field traps the droplet. We note that analogous solutions exist for circular orbits at high wave memory, where the orbital radius r_0 satisfies the quantization $J_0(k_F r_0) = 0$.[15,25,26,45,46] The periodic wave-trapped solutions of interest here are a version of these "hydrodynamic spin states" for motion confined to a line.

In Fig. 8, we plot the wave profile over time for two periods of a periodic wave-trapped solution at high memory M_e [as defined in Eq. (8)], which is a more useful measure of the vibrational forcing in the limit $\Gamma \to \Gamma_F^-$. Strikingly, we observe that at high memory, the wave at each impact $\eta_0(x, t_n)$ differs from the mean wave field $\bar{\eta}_0(x)$ only by a small perturbation. The unstable nature of this periodic state

is emphasized by the fact that $\bar{\eta}_0(x)$ decreases rapidly for $|x| \gtrsim \mathcal{A}$, which is to say that the droplet could escape the potential trap imposed by its mean wave field for sufficiently large perturbations.

From Fig. 9(a), we observe that the amplitude $\mathcal{A}$ of the periodic oscillation decreases as the wave memory M_e increases, while the oscillation period $\mathcal{P}$ attains a minimum value before increasing at high vibrational forcing. We rationalize these dependencies in terms of the effective potential induced by the mean wave field. By applying Corollary 1, we use the convolution result to obtain the mean wave field $\bar{\eta}_0(x)$ over one period of the oscillatory motion, with results shown in Fig. 9(b). As M_e increases, $\bar{\eta}_0(x)$ becomes increasingly flat for $|x| \leq \mathcal{A}$, resulting in a decrease in the propulsive force
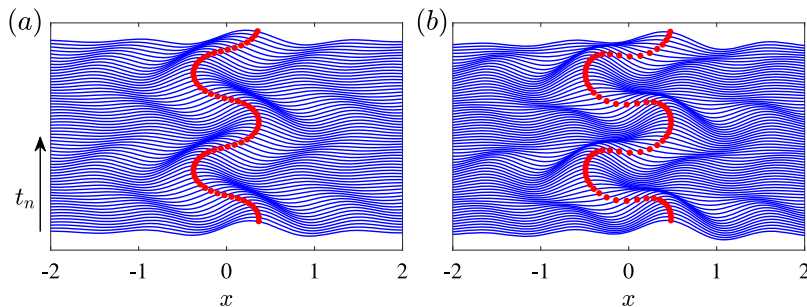

FIG. 5. The evolution of the wave field $\eta_0(x, t_n)$ (blue curves) and droplet position X_n (red dots) at impact over two periods of the computed (stable) periodic states. (a) $\Gamma/\Gamma_F = 0.90$ and $\tilde{\kappa} \approx 0.066$. (b) $\Gamma/\Gamma_F = 0.96$ and $\tilde{\kappa} \approx 0.037$.
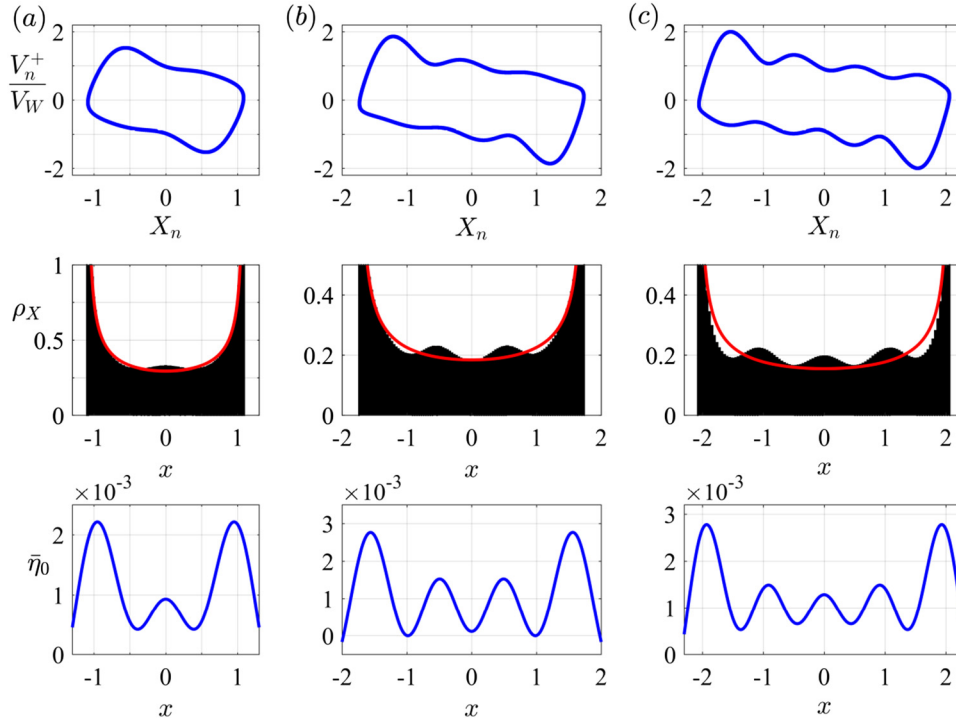
FIG. 6. Simulated periodic dynamics. Top row: Phase plane orbits for $\tilde{\kappa} = 0.012$, where the velocity is normalized by the free walking speed V_W.[15] Middle row: Stationary probability distributions for the droplet position $\rho_X(x)$ (black) and that of the simple harmonic oscillator (red) for the corresponding amplitude $\mathcal{A}$. Bottom row: The corresponding mean wave field $\bar{\eta}_0(x)$ as computed by the convolution $\bar{\eta}_0 = \rho_X * \eta_B$. The columns correspond to the values of Γ/Γ_F in Fig. 4, with (a) $\Gamma/\Gamma_F = 0.90$, (b) $\Gamma/\Gamma_F = 0.94$, and (c) $\Gamma/\Gamma_F = 0.96$.

provided by the mean wave field. This reduces the average droplet speed, and thus the oscillation period $\mathcal{P}$ increases. Furthermore, the steepness of the stationary cumulative probability distribution $\mathcal{C}_X(x)$ at high vibrational forcing for $|x| \approx \mathcal{A}$ [see Fig. 9(c)] indicates that the droplet spends a significant portion of the oscillation bouncing near its maximum range, which further increases the oscillation period.

To postulate a lower bound of the oscillation amplitude $\mathcal{A}$ in the high memory limit, we exploit the fact that the droplet spends significant time near its oscillation extrema [see Fig. 9(c)], and so approximate its probability density function

by $\rho_X(x) \approx \frac{1}{2}[\delta(x + \mathcal{A}) + \delta(x - \mathcal{A})]$. An application of Corollary 1 thus yields $\bar{\eta}_0(x) \approx \frac{1}{2}[\eta_B(x + \mathcal{A}) + \eta_B(x - \mathcal{A})]$. For oscillatory motion to persist, it is natural to require that the extremum at $x = 0$ is a local minimum, corresponding to $\bar{\eta}_0''(0) > 0$, or equivalently, $\eta_B''(\mathcal{A}) \gtrsim 0$. A second natural requirement is for $\bar{\eta}$ to slope inwards at the point of maximum oscillation amplitude, corresponding to $\bar{\eta}_0'(\mathcal{A}) > 0$ (by the symmetry of $\bar{\eta}_0$), or equivalently, $\eta_B'(2\mathcal{A}) \gtrsim 0$. From the computation of $\eta_B(x)$ in the limit $M_e \to \infty$ (as depicted in Fig. 2), the two conditions on η_B are both satisfied for $0.3 \lesssim \mathcal{A} \lesssim 0.5$; we thus postulate that $\mathcal{A} \approx 0.3$ is a lower bound for the amplitude of periodic wave-trapped solutions as $M_e \to \infty$ [see Fig. 9(a)], a limit prescribed by the length scale of the Faraday waves.

Although the wave-trapped solutions are unstable in the parameter regime explored experimentally, they demonstrate that in the high memory limit, the mean Faraday wave field may trap the droplet in periodic motion. In a sense, the mean wave field $\bar{\eta}$ then acts as a potential, related by Corollary 1 to the droplet's statistical distribution through $\bar{\eta}_0 = \rho_X * \eta_B$. Hence, the periodic motion of the droplet is in effect driven by its own stationary probability distribution ρ_X. We re-explore this concept in Sec. IV C for the case of chaotic dynamics in the high memory limit.
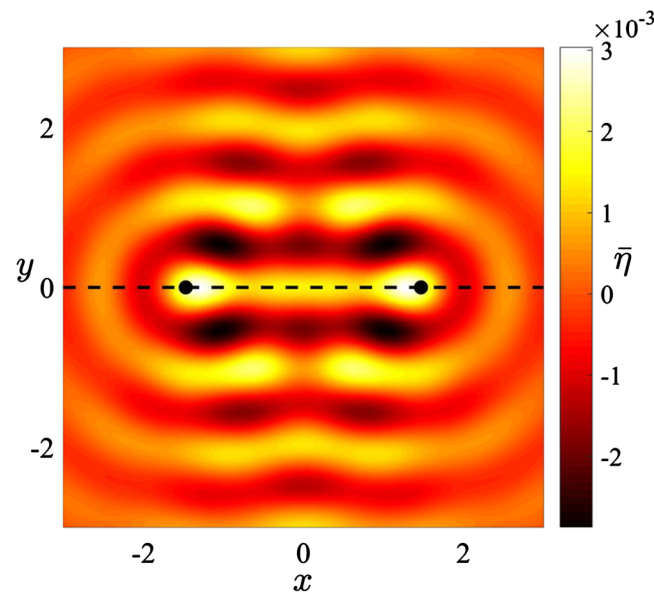

FIG. 7. Mean 3-dimensional wave field $\bar{\eta}(\boldsymbol{x})$ for stable periodic dynamics at $\Gamma/\Gamma_F = 0.96$, where $\boldsymbol{x} = (x, y)$. The circles indicate the oscillation amplitude $\mathcal{A} \approx 1.47$.

IV. CHAOTIC DYNAMICS

We now consider the chaotic dynamics arising at sufficiently high memory that the periodic states destabilize via the Ruelle-Takens-Newhouse scenario (Sec. IV A). In the high memory limit, we rationalize the form of the chaotic dynamics and emergent statistics (Sec. IV B) and propose a stochastic reformulation of the pilot-wave dynamics (Sec. IV C).
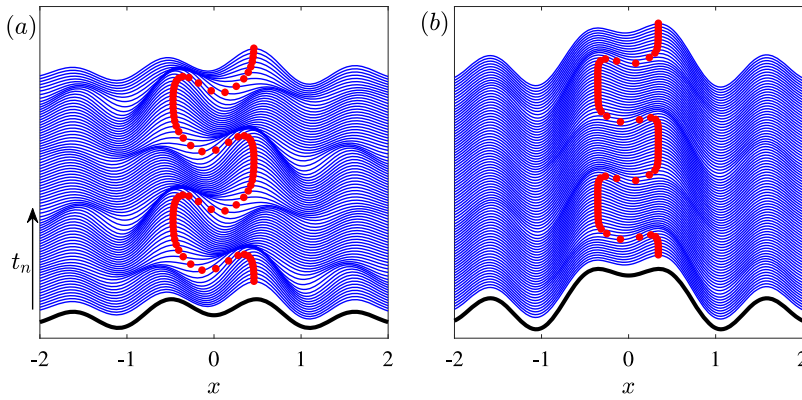
FIG. 8.   Computed periodic wave-trapped solutions arising in the absence of a central force ($\tilde{\kappa} = 0$). The impact wave field $\eta_0(x, t_n)$ (blue curves) and droplet position X_n (dots) are shown over two oscillation periods for $\mathcal{P} = 42$. The black curve is the corresponding mean wave field $\bar{\eta}_0(x)$. The wave memory is (a) $M_e \sim 47.7$ (corresponding to $\Gamma / \Gamma_F = 0.985$) and (b) $M_e \sim 4.78 \times 10^3$. We note that as M_e increases, the instantaneous wave field $\eta_0(x, t_n)$ approaches its mean $\bar{\eta}_0(x)$ at all times.

A. Transition to chaos

As Γ is increased, the periodic phase-plane orbits may destabilize into regular wobbling orbits, before transitioning to chaos. The route to chaos for circular orbits in a harmonic potential has been explored experimentally[28,47] and theoretically[48] using the stroboscopic trajectory equation.[42] In both cases, the Ruelle-Takens-Newhouse route to chaos[32,33] was observed. According to this scenario, from a fixed point, three bifurcations induce additional incommensurate frequencies into the spectrum, after which it is *likely* (but not guaranteed) that a strange attractor appears in the phase space.[49]

Following the methodology of Tambasco *et al.*,[48] we fix $\tilde{\kappa} = 0.03$ and initialize a simulation for a value of Γ where the periodic motion is stable, as indicated by the linear stability analysis. The simulation runs for $N_0 + 2^p$ impacts, where the first N_0 impacts are discarded to remove transient effects. We take the Fourier transform of the droplet position X_n for the final 2^p impacts (typically $p = 17$) and locate the frequencies f corresponding to the peaks in the power spectrum P. At the end of the simulation, we increment $\Gamma \mapsto \Gamma + \Delta(\Gamma / \Gamma_F)\Gamma_F$, where $\Delta(\Gamma / \Gamma_F)$ is chosen adaptively to capture the bifurcations.

The fixed point of this system is a bouncer at the origin, which destabilizes via a Neimark-Sacker bifurcation (bifurcation B1), as discussed in Sec. III A. Beyond this threshold, the frequency spectrum of the resulting stable limit cycle is dominated by $f_1 = 1/\mathcal{P}$ and its harmonics, where $\mathcal{P} \approx 63$ is as computed in Sec. III. This is highlighted by the frequency spectrum in Fig. 10(a) with accompanying phase portraits and probability density functions. At $\Gamma / \Gamma_F \approx 0.980447$ (B2), this motion destabilizes through the emergence of complex conjugate unstable eigenvalues with oscillatory frequency $f_2^\star$

[see Fig. 10(b)]. The resulting instability is saturated by nonlinear effects, leading to the quasi-periodic stable wobbling motion with incommensurate frequencies f_1 and $f_2 \approx f_2^\star$ and their integer combinations [see Fig. 11(a)]. This evolution invokes a qualitative change in the statistics, with several peaks emerging in the droplet position stationary distribution [Fig. 10(b)]. Unlike the route to chaos of circular orbits,[48] we do not observe any frequency locking between f_1 and f_2.

For $\Gamma / \Gamma_F \gtrsim 0.98050$, a third bifurcation (B3) yields the incommensurate frequency f_3, as is typical of the Ruelle-Takens-Newhouse route to chaos[32,33] [see Fig. 10(c)]. While several additional peaks arise in the frequency spectrum following this bifurcation, the dynamics are still dominated by the frequencies f_1 and f_2 (and their harmonics), yielding a qualitatively similar probability distribution. For $\Gamma / \Gamma_F \gtrsim 0.980594$ (B4), additional peaks emerge in the probability distribution and the phase-portrait appears less regular [Fig. 10(d)]. In particular, the broad-banded frequency spectrum suggests chaotic dynamics, which we verify by considering the Lyapunov exponent. We follow Gilet[20,50] and consider two simulations from the same initial conditions, except for an initial perturbation in the dimensionless droplet position of 10^{-10}, yielding trajectories $X^{(1)}(t)$ and $X^{(2)}(t)$. As shown in Fig. 11(b), the difference $\chi \equiv |X^{(1)} - X^{(2)}|$ oscillates in the interval $10^{-11} \lesssim \chi \lesssim 10^{-6}$ just before B4 ($\Gamma / \Gamma_F = 0.980593$), but grows to be of order 1 just after B4 ($\Gamma / \Gamma_F = 0.980594$), indicating a positive Lyapunov exponent and the onset of chaos.

B. The high memory limit

We now consider the high memory regime ($M_e \gtrsim 10^3$) in which there is a qualitative change in the dynamics.
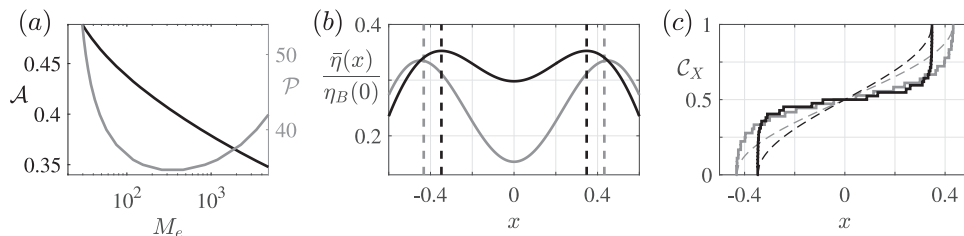

FIG. 9.   (a) Amplitude $\mathcal{A}$ (black) and period $\mathcal{P}$ (gray) of periodic wave-trapped solutions as a function of the memory M_e. (b) The mean wave field $\bar{\eta}(x)$ relative to the bouncer wave field $\eta_B(0)$. The vertical dashed lines denote the corresponding drop oscillation amplitude $\mathcal{A}$. (c) The corresponding stationary cumulative probability distribution $\mathcal{C}_X(x) = \int_{-\mathcal{A}}^{x} \rho_X(s) \, ds$ for periodic wave-trapped solutions (solid lines) and for simple harmonic motion with amplitude $\mathcal{A}$ (dashed lines). In (b) and (c), the gray curves correspond to $M_e \sim 47.7$, $\mathcal{P} = 36$, and $\mathcal{A} \approx 0.43$, and the black curves correspond to $M_e \sim 4.8 \times 10^3$, $\mathcal{P} = 42$, and $\mathcal{A} \approx 0.35$.
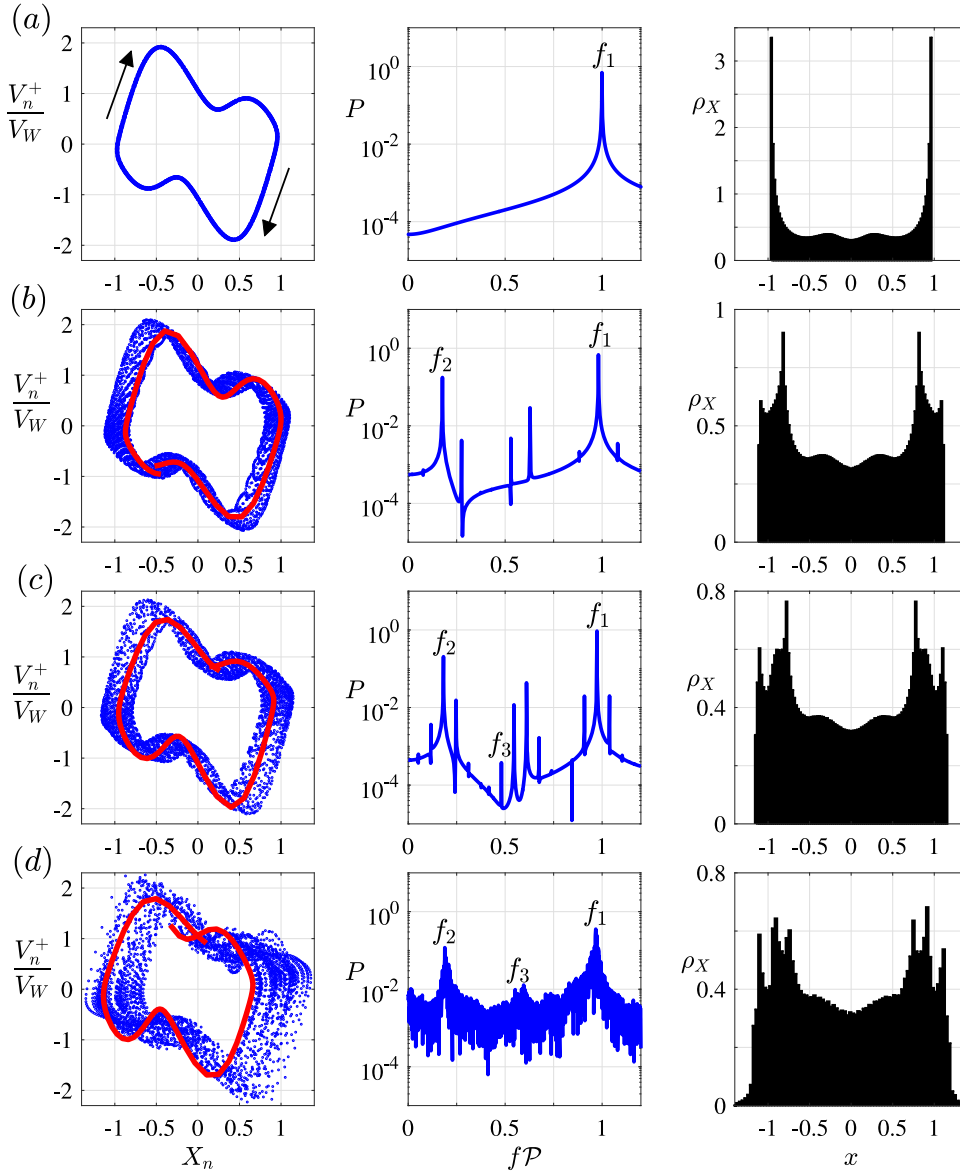
FIG. 10. Route to chaos. The columns present the simulated phase plane behavior (left), power spectrum (middle), and probability density function (right) during the transition to chaos. Γ/Γ_F increases with each row: (a) periodic motion ($\Gamma/\Gamma_F = 0.98044$), (b) two-frequency quasi-periodic motion ($\Gamma/\Gamma_F = 0.98048$), (c) three-frequency quasi-periodic motion ($\Gamma/\Gamma_F = 0.98056$), and (d) chaotic motion ($\Gamma/\Gamma_F = 0.980594$). In the phase-plane plots (left column), the blue dots denote the prior 5000 impacts, and the red lines the final $\mathcal{P}$ impacts in the nonperiodic cases. The walker velocity V_n^+ is normalized by the free walking speed V_W at the corresponding value of Γ/Γ_F.[15]

Specifically, the wave field dominates the harmonic potential so that the droplet may change the direction several times before crossing the origin, as indicated in Fig. 12. We find that the mean Faraday wave field plays a crucial role in these chaotic dynamics, giving rise to a jump-like process between a discrete set of points, the locations of which we rationalize in Sec. IV B1. In Secs. IV B2 and IV B3, we see the emergence of wavelike statistics, where the peaks correspond to the discrete turning points of the droplet motion. We then use the relationship between the droplet statistics and the mean wave field (Theorem 1) to postulate an effective potential $\mathcal{V}_e(x)$ that influences the chaotic motion of the droplet (Sec. IV C). The additional notation used throughout this section is summarized in Table II.

To gain further understanding of the pilot-wave dynamics in this regime, it is useful to recast the iterative map (5)–(7) as a trajectory equation for the droplet position X_n and the mean droplet velocity during flight $U_n \equiv X_{n+1} - X_n$. By computing the droplet fundamental matrix $\boldsymbol{F}(\tilde{\kappa})$ analytically,

the droplet's evolution may be expressed as

$$X_n - X_{n-1} = U_{n-1}, \tag{13}$$

$$(U_n - U_{n-1}) + \mathfrak{D}U_{n-1} = -\partial_x \mathcal{V}_p(x, t_n)|_{x=X_n}, \tag{14}$$

where $\mathfrak{D} = 1 - (1 - F)e^{-\tilde{v}_p}$ is a drag coefficient, and

$$\mathcal{V}_p(x, t_n) = \tfrac{1}{2}\mathfrak{K}x^2 + \mathfrak{F}\eta_0(x, t_n) \tag{15}$$

is the time-dependent full pilot-wave potential, which is the sum of the applied harmonic potential and the wave field at each impact. In the vicinity of the origin ($|x| \lesssim 3$ in Fig. 12), the full pilot-wave potential at each impact $\mathcal{V}_p(x, t_n)$ oscillates in x. However, as $|x| \to \infty$ the instantaneous wave field decays and we observe that $\mathcal{V}_p(x, t_n) \approx \tfrac{1}{2}\mathfrak{K}x^2$ for all time. In (15), $\mathfrak{K}(\tilde{\kappa}) > 0$ determines the strength of the time-averaged harmonic potential over one impact period and $\mathfrak{F}(\tilde{\kappa}) > 0$ prescribes the magnitude of the wave force (whose dependence
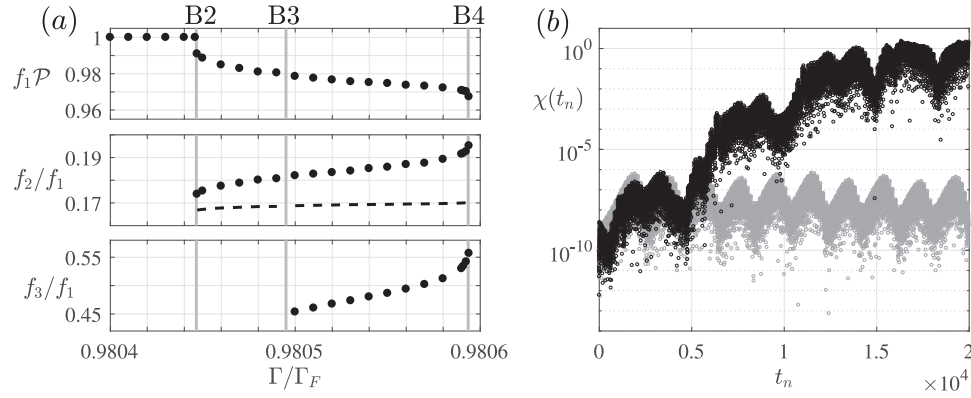
FIG. 11. Route to chaos. (a) Fundamental frequencies f_1, f_2, and f_3 (dots) are introduced with successive bifurcations B2–B4 (gray) as the memory is progressively increased. The bifurcation B1 from stationary bouncing to orbiting occurs at $\Gamma/\Gamma_F \approx 0.81$ and is not shown in this figure. The periodic motion has period $\mathcal{P}$, where $\mathcal{P} = 1/f_1$ for stable dynamics (before bifurcation B2). After B2, the periodic orbit is unstable with linear instability frequency $f_2^\star$ (dashed line). (b) The difference $\chi(t) \equiv |X^{(1)}(t) - X^{(2)}(t)|$ between two trajectories $X^{(1)}$ and $X^{(2)}$ (whose initial position differ by a dimensionless distance of 10^{-10}) is shown for $\Gamma/\Gamma_F = 0.980593$ (gray) and $\Gamma/\Gamma_F = 0.980594$ (black). These values of Γ correspond, respectively, to 3-frequency quasi-periodic motion and chaotic dynamics.

on $\tilde{\kappa}$ is weak).[51] The system (13) and (14) and the full pilot-wave potential $\mathcal{V}_p$ will be referred to throughout Secs. IV B and IV C.

1. The random walk dynamics

In Fig. 12, we plot the evolution of the full pilot-wave potential $\mathcal{V}_p(x, t_n)$ and the corresponding droplet position X_n at successive impacts in the high memory regime. To understand the role of the long-lived Faraday waves in this regime, we plot the spatial minima of $\mathcal{V}_p(x, t_n)$ at each impact, from which two important observations emerge. First, the minima far from the droplet (typically $\gtrsim 1$ Faraday wavelength away) remain at a roughly constant position over time, indicating
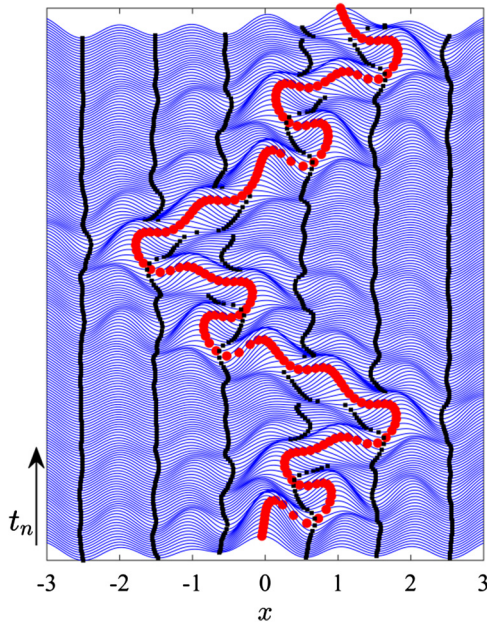
the potential has an underlying stationary structure induced by the wave field. Second, when the droplet changes direction (at which point it is moving slowly), the local-pilot wave accumulates, increasing the droplet's potential energy, from which the droplet departs and heads towards one of the neighboring potential minima. Depending on the prior dynamics, the droplet will turn around again at one of the minima of $\mathcal{V}_p(x, t_n)$ on its path.

To analyze these dynamics, we define the set of turning times $\mathcal{T} \subset \mathbb{N}$ to be the times at which the droplet changes direction. That is to say, if $\tau_i \in \mathcal{T}$, then $X(\tau_i)$ is a local extremum and $T_i \equiv X(\tau_i)$ is defined to be a turning point. In the droplet trajectory time-series data in Fig. 13(a), the turning times τ_i and positions T_i correspond to the red dots. Furthermore, it appears that the droplet changes position only in the vicinity of specific points on the bath and that there is an apparent structure to the distance between turning points $D_i = |T_{i+1} - T_i|$. Indeed, by plotting the distribution ρ_D of distances D_i [see Fig. 13(b)], it emerges that the distance between turning points is quantized, where ρ_D has sharp maxima at points approximated by the set

$$\mathcal{D} = 0.6 + \mathbb{N} \equiv \{0.6, 1.6, 2.6, \ldots\}.$$

The emergence of this quantization lies in the combined structure of the global standing wave field and the wave field generated by the droplet at each impact, whose shape is

FIG. 12. Pilot-wave dynamics at high memory ($M_e \sim 1.17 \times 10^4$ with $\tilde{\kappa} = 0.01$). Droplet trajectory X_n (red dots) and the full pilot-wave potential $\mathcal{V}_p(x, t_n)$ (blue curves), which is the sum of the harmonic potential and the wave field, as defined in Eq. (15). The black squares denote the spatial minima of $\mathcal{V}_p(x, t_n)$.

TABLE II. Additional notation used throughout Sec. IV B.

| Variable	Description
$\tau_i \in \mathcal{T}$	Turning times (raw data)
$T_i \equiv X(\tau_i)$	Turning positions (raw data)
$C(t)$	Trend curve on the slow timescale
X_n^R	Residual droplet impact positions
T_i^R	Residual turning positions
$\rho_X(x)$	Probability distribution of X_n (raw data)
$\rho_T(x)$	Probability distribution of T_i (raw data)
$\rho_{XR}(x)$	Probability distribution of X_n^R (residuals)
$\rho_{TR}(x)$	Probability distribution of T_i^R (residuals)
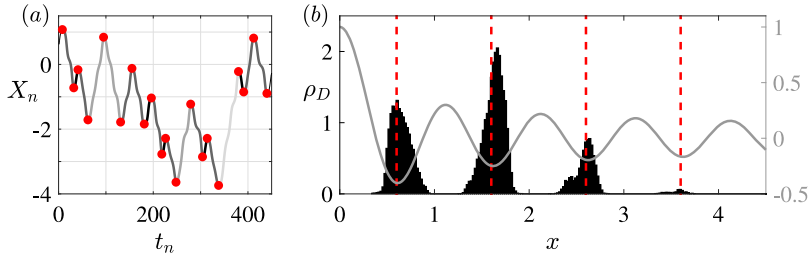
FIG. 13. The random walk-like dynamics in the wave-dominated, high memory regime. (a) Example trajectory X_n over a short time interval for $\tilde{\kappa} = 0.01$ and $M_e \sim 1.17 \times 10^4$. Red dots denote the times τ_i and positions $T_i \equiv X(\tau_i)$ at which the droplet changes direction. The four shades of gray indicate the four typical distances between turning points observed. (b) Histogram ρ_D of the distance between turning points (black). The vertical lines (red dashed) indicate the values in $\mathcal{D} = \{0.6, 1.6, 2.6, \ldots\}$, and the gray curve is $J_0(k_F x)$.

approximated by $J_0(k_F x)$. From the observations in Fig. 12, it becomes clear that it is the minima of $J_0(k_F x)$ that plays a role in prescribing the quantized distance between turning points, with values in the set $\mathcal{D}$. This correspondence is shown in Fig. 13(b). In what follows, we rationalize these dynamics by considering a jump process, before postulating a stochastic model in Sec. IV C.

We proceed by presenting a simple geometric argument that demonstrates the role of the quantized distance between turning points in the long-time statistics. We consider a Markovian jump process $(x_n)_{n \geq 0}$ between turning points, where the jump distances $d_n \equiv |x_n - x_{n-1}|$ are *exactly* restricted to $d_n \in \mathcal{D}$. In accordance with our observations of the pilot-wave system in the high memory limit (see Figs. 12 and 13), we require that the set of possible points visited by the jump process forms a communicating class with symmetry preserved about the origin.

We denote $\alpha \in \mathbb{R}$ as a position visited by the jump process (whose possible values are determined in the following analysis), and without loss of generality, we set $x_0 = \alpha$ and consider $x_1 > x_0$. Using the assumed structure of $\mathcal{D} = 0.6 + \mathbb{N}$, we define $N_n \in \mathbb{N}$ such that $d_n = 0.6 + N_n$. As the droplet changes direction at each turning point, we observe that after an even number of jumps

$$|x_{2n} - x_0| = \left| \sum_{i=1}^{2n} (-1)^{i+1}(0.6 + N_i) \right| = \left| \sum_{i=1}^{2n} (-1)^{i+1} N_i \right|,$$

so $|x_{2n} - x_0| \in \mathbb{N}$ for all $n \in \mathbb{N}$. By a similar calculation, we find that after an odd number of jumps

$$|x_{2n+1} - x_0| \in \begin{cases} 0.6 + \mathbb{N} & \text{if } x_{2n+1} > x_0 = \alpha, \\ 0.4 + \mathbb{N} & \text{if } x_{2n+1} < x_0 = \alpha. \end{cases}$$

Thus, for all points in the jump process to form a communicating class, we require $x_n \in \mathcal{M}(\alpha)$ for all $n \geq 0$, where α

parametrizes the mesh

$$\mathcal{M}(\alpha) = \{\ldots, \alpha - 1.4, \alpha - 1, \alpha - 0.4, \alpha,$$
$$\alpha + 0.6, \alpha + 1, \alpha + 1.6, \ldots\}. \quad (16)$$

We note that this mesh is periodic with period 1, so without loss of generality, we restrict the displacement of the mesh to $\alpha \in [-\frac{1}{2}, \frac{1}{2})$. For symmetric statistics about the origin, we require that α be such that $\mathcal{M}(\alpha)$ is also symmetric, which yields $\alpha \in \{-0.3, 0.2\}$. For consistency with the jump distances $d_n \in \mathcal{D}$, the droplet may only leave each mesh point in a fixed direction (as depicted in Fig. 14), namely, to the right for $x_n \in \alpha + \mathbb{Z}$ and to the left for $x_n \in \alpha + 0.6 + \mathbb{Z}$.

2. Detrending the long-time statistics

From the analysis in Sec. IV B 1, we expect the turning points T_i (and the peaks of the corresponding probability distribution ρ_T) to be determined by the meshes $\mathcal{M}_0 = \mathcal{M}(0.2)$ and $\mathcal{M}_1 = \mathcal{M}(-0.3)$, where

$$\mathcal{M}_0 = \{\ldots, -1.2, -0.8, -0.2, +0.2, +0.8, +1.2, \ldots\},$$
$$\mathcal{M}_1 = \{\ldots, -1.3, -0.7, -0.3, +0.3, +0.7, +1.3, \ldots\},$$

and $\mathcal{M}_0$ is a translation of $\mathcal{M}_1$ by $1/2$. The jump lengths $d_n \in \mathcal{D}$ impose a unique direction to leave each mesh point, yielding qualitatively different dynamics, as highlighted by the schematic diagram in Fig. 14. Due to the finite width of the distribution ρ_D about each of its modes [with typical value $\lesssim 0.25$ — see Fig. 13(b)], there is a corresponding finite width in the turning point distribution about each predicted mesh point. Hence, these distributions may overlap for mesh points spaced 0.4 apart but are well separated for mesh points spaced 0.6 apart. In the turning points' time series, this yields a thicker "band structure" between mesh points spaced 0.4 apart, as seen in Fig. 15(a), where the central mesh points are visited most frequently. By symmetry, we expect the central
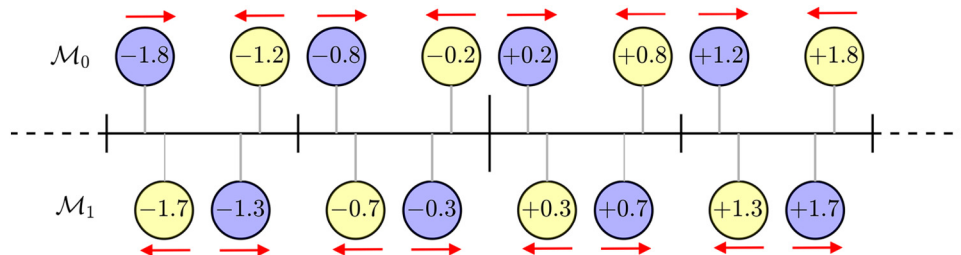

FIG. 14. Schematic diagram for a subset of mesh points for $\mathcal{M}_0$ (top row) and $\mathcal{M}_1$ (bottom row), where both meshes are periodic with period 1 and $\mathcal{M}_0$ is a translation of $\mathcal{M}_1$ by $1/2$. The jump distance must lie in $\mathcal{D}$, where turning points necessitate a change in direction after each jump. This evolution is equivalent to leaving each point in the direction of the arrow and changing color at each jump (blue/yellow). The relationship between the random walk dynamics and the derived effective potential $\mathcal{V}_e(x)$ is evident in Fig. 18.
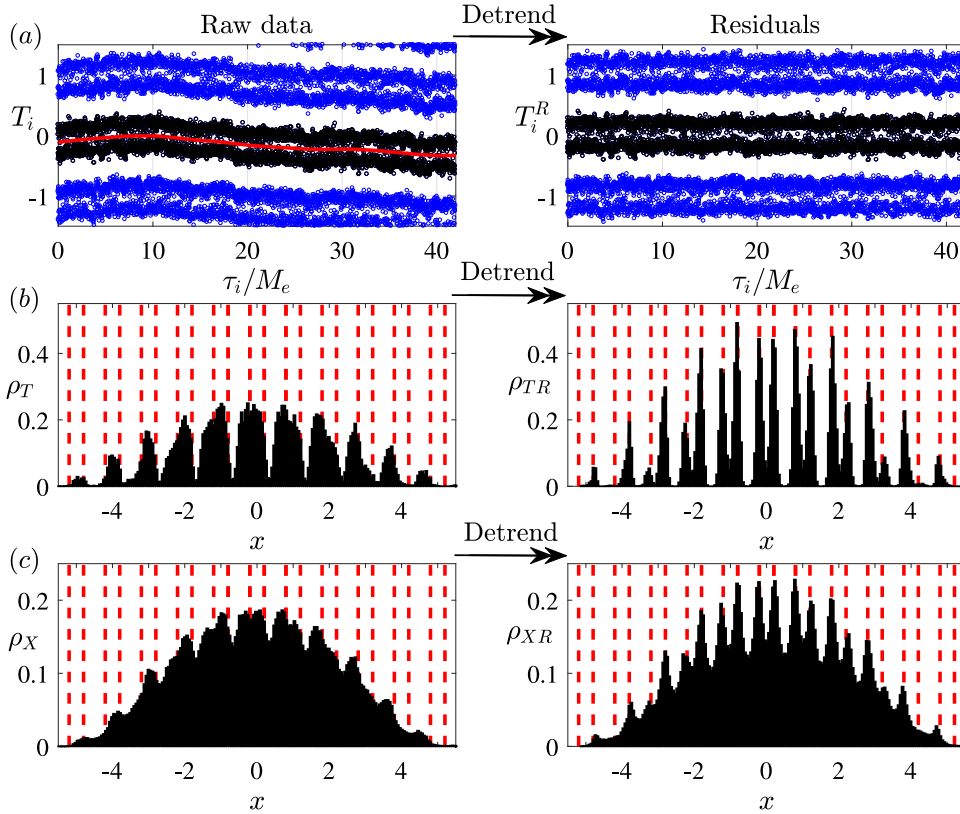
FIG. 15. Detrending of the slow timescale drift that arises in the random walk-like motion. The left column shows the raw simulation data, while the right column shows the residuals after subtracting out the slow drift $C(t)$. (a) Zoom in of the turning point time series $T_i \equiv X(\tau_i)$ (circles) for $\tilde{\kappa} = 0.005$ and $M_e \sim 1.17 \times 10^4$. The trend curve C (red) is fitted to the black circles only (this is the subset $\mathcal{S} \subset \mathcal{T}$ defined in Appendix D). After detrending (right panel), the bands are approximately constant in time. (b) The distribution of all turning points T_i before (ρ_T, left panel) and after (ρ_{TR}, right panel) detrending. (c) The distribution of all impact positions X_n before (ρ_X) and after (ρ_{XR}) detrending. The red dashed lines in (b) and (c) correspond to the mesh points of $\mathcal{M}_0$ (see Fig. 14); following detrending, the peaks of ρ_{TR} and ρ_{XR} both align with the mesh points of the random walk.

band $[-0.2, 0.2]$ to dominate the statistics in the case of $\mathcal{M}_0$ but the two bands $[-0.7, -0.3]$ and $[0.3, 0.7]$ to be equally dominant for $\mathcal{M}_1$.

Our study reveals an additional complication; specifically, the finite width about the peaks in ρ_D allows for a slow translation in the dominant turning point locations, as is evident in Fig. 15(a). The translation occurs on a slow timescale, comparable to the memory time M_e, the timescale at which the global wave field structure changes. This drift obscures the structure of the underlying statistics induced from the short-time dynamics; for example, there is only a weak structure apparent in the distribution of turning points ρ_T in Fig. 15(b).

To remedy this, we *detrend* the time-series data using statistical methods and then analyse the residuals. This detrending involves finding a smooth best fit $C(t)$ for the time varying drift and re-expressing the variation in the data about

$C(t)$. This technique visibly enhances the wavelike nature of the droplet's statistical distribution [see Figs. 15(b) and 15(c)] and allows us to compare the resultant dynamics to the predicted random walk meshes $\mathcal{M}_0$ and $\mathcal{M}_1$. The details of the statistical techniques used are given in Appendix D.

3. Results

We now explore the statistical distributions following the detrending of the slow timescale dynamics. By defining $R(t) \equiv X(t) - C(t)$, we have impact residuals $X_n^R \equiv R(t_n)$ for all $n \geq 0$ and turning point residuals $T_i^R \equiv R(\tau_i)$ for all $\tau_i \in \mathcal{T}$, with respective residual probability distributions ρ_{XR} and ρ_{TR}. We demonstrate that the distribution modes vary with the relative strength of the central and wave forces, and are intrinsically linked to the mean wave field $\bar{\eta}_0(x)$ and an associated effective potential $\mathcal{V}_e(x)$ to be defined in Sec. IV C.
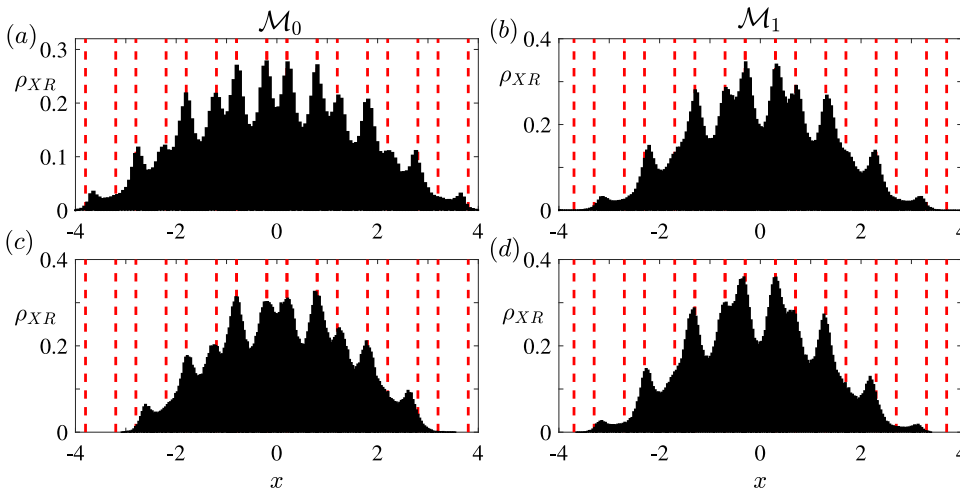

FIG. 16. Histograms ρ_{XR} of the residual system X_n^R. In (a) and (c), we fix $M_e \sim 1.17 \times 10^4$ and vary $\tilde{\kappa}$, with (a) $\tilde{\kappa} = 0.01$ and (c) $\tilde{\kappa} = 0.02$. The modes of both histograms $\rho_{XR}(x)$ correspond to the mesh $\mathcal{M}_0$. In (b) and (d), we fix $\tilde{\kappa} = 0.01$ and vary M_e, with (b) $M_e \sim 2.89 \times 10^3$ and (d) $M_e \sim 1.97 \times 10^3$. In this case, the modes of $\rho_{XR}(x)$ now correspond to $\mathcal{M}_1$.
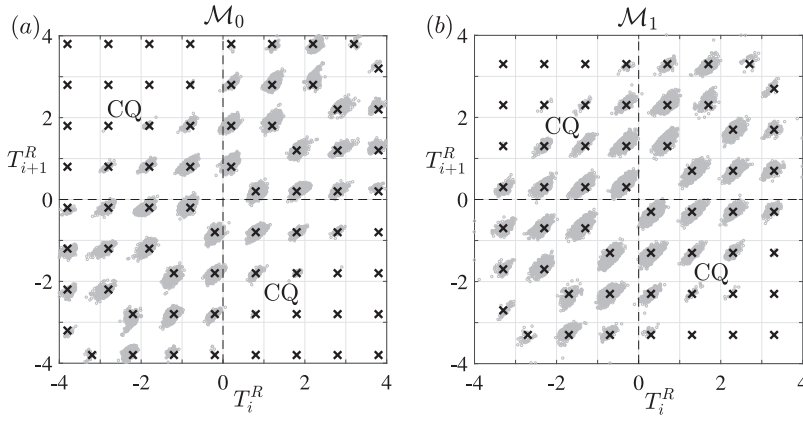
FIG. 17. Behavior of successive residual turning points T_i^R, with simulation data plotted for $\tilde{\kappa} = 0.01$ with (a) $M_e \sim 1.17 \times 10^4$ and (b) $M_e \sim 2.89 \times 10^3$ (gray circles). The black crosses give the possible combinations of successive turning points as prescribed by the associated mesh, with (a) $\mathcal{M}_0$ and (b) $\mathcal{M}_1$ (see Fig. 14). The droplet crosses the origin between crossing quadrants (CQ), in which either $T_i^R > 0$ and $T_{i+1}^R < 0$, or $T_i^R < 0$ and $T_{i+1}^R > 0$.

Examples of the corresponding residual distributions are given in Figs. 15(b) and 15(c), where the residual statistics are symmetric relative to mesh $\mathcal{M}_0$. The modes of ρ_{XR} correspond to the modes of ρ_{TR} since the droplet is moving slowest at the turning points, so spends most of its time in their vicinity. The harmonic potential dominates the wave field far from the origin, which explains the slight discrepancy between the distribution modes and the mesh points for large $|x|$. We note that the sub-mesh points $\{\pm 1.2, \pm 2.2, \ldots\}$ are visited less frequently as these drive the droplet away from the origin (see Fig. 14), countering the harmonic potential.

To explore the extent of the random walk-like dynamics, we vary the parameters $\tilde{\kappa}$ and M_e and present the results in Fig. 16. When M_e is fixed, the quantization is sharper when the waves dominate the harmonic potential [Fig. 16(a)], but as $\tilde{\kappa}$ is increased, the peaks become broader and the quantization loses clarity [Fig. 16(c)]. The plot of successive turning points [Fig. 17(a)] confirms that the droplet motion is consistent with the directional arrows predicted by the mesh $\mathcal{M}_0$ (see Fig. 14). However, it is relatively rare for the droplet to cross the centre of the bath (corresponding to $T_i^R T_{i+1}^R < 0$), a feature that we rationalize in Sec. IV C.

When the wave memory M_e is reduced (with $\tilde{\kappa}$ fixed), the random walk-like dynamics shift to the $\mathcal{M}_1$ mesh, where the sub-mesh $\{\pm 0.3, \pm 1.3, \ldots\}$ dominates the distribution modes [see Figs. 16(b) and 16(d)]. Although the mesh points $\{\pm 0.7, \pm 1.7, \ldots\}$ remain apparent in the residual turning point distribution ρ_{TR} [Fig. 17(b)], their presence is obscured in ρ_{XR} [Fig. 16(b)]. As M_e is further decreased, the mesh points that counter the harmonic potential ($\{\pm 0.7, \pm 1.7, \ldots\}$) are visited less frequently [Fig. 16(d)]. Indeed, it appears from Fig. 17(b) that the centre of the bath is crossed more frequently in this regime, as the relative strength of the central force is more pronounced at lower wave memory.

These random walk-like dynamics differ substantially from those arising in a bath driven at two incommensurate

frequencies[52] and those in a corral given by the toy model of Gilet.[20,50] In our case, the domain is unbounded, so the allowable steps between turning points are dominated by the structure of the droplet's local wave field. The associated random walk mesh ($\mathcal{M}_0$ or $\mathcal{M}_1$) is selected by the relative strength of the central and wave forces, where the mesh $\mathcal{M}_0$ is dominant in the high memory limit. In contrast, the random walk-like motion observed by Gilet is instead induced by the global wave field given by the corral's cavity modes, with a fixed random walk step size of $\lambda_F/2$.

C. The mean-pilot-wave potential

Based on the ideas of Theorem 1, we start by considering an effective potential $\mathcal{V}_e(x)$ using the stationary residual distribution $\rho_{XR}(x)$ and the applied harmonic potential $\frac{1}{2}\mathfrak{K}x^2$, defining $\mathcal{V}_e(x) = \frac{1}{2}\mathfrak{K}x^2 + \mathfrak{F}(\rho_{XR} * \eta_B)(x)$. Remarkably, the direction associated with each mesh point (as given by Fig. 14) corresponds precisely to the gradients of $\mathcal{V}_e$, as indicated by the arrows in Fig. 18. This correspondence provides a strong indicator that the chaotic motion of the droplet is driven by an effective potential induced by the slow decay of the pilot-wave field in the high memory limit. With this observation in mind, we sketch a stochastic reformulation of the long-time pilot-wave dynamics in the high memory limit, from which we aim to derive an equation for the time-dependent probability distribution $\rho(x, t)$ for the droplet's position.

Following a similar idea to that proposed by Labousse et al.,[30] we decompose the pilot-wave dynamics using its contrasting short and long timescale behavior. Specifically, we model the contribution of the wave field to the pilot-wave dynamics in terms of a propulsive nonlinear drag $-D(U_n)U_n$ (similar to that used in the weak acceleration limit),[43,44] an approximation for the effect of the long-lived Faraday waves, and a mean-zero normally distributed random noise
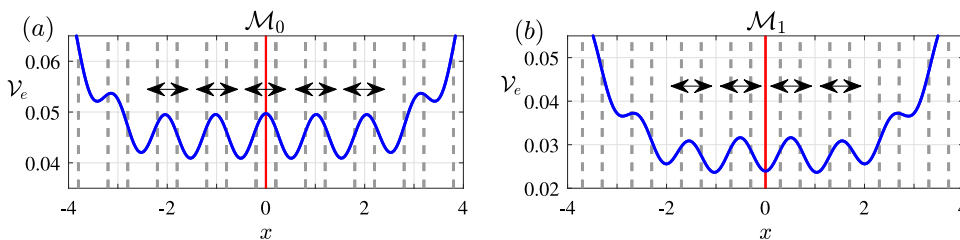

FIG. 18. Effective potential $\mathcal{V}_e(x)$ (blue) with $\tilde{\kappa} = 0.01$ for (a) $M_e \sim 1.17 \times 10^4$ (corresponding to mesh $\mathcal{M}_0$) and (b) $M_e \sim 2.89 \times 10^3$ (corresponding to mesh $\mathcal{M}_1$). The vertical gray dashed lines and the arrows indicate the mesh points and corresponding directions as given by the schematic diagram in Fig. 14. The potentials are symmetric about $x = 0$ (red line).
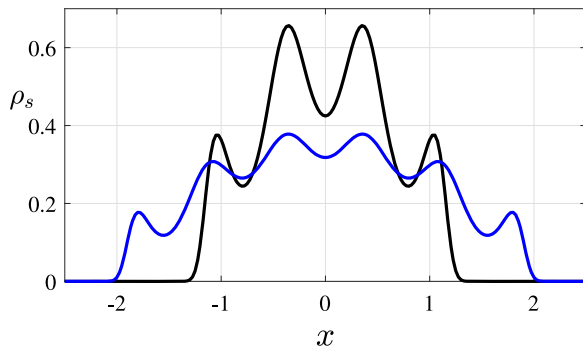
FIG. 19. Solution $\rho_s(x)$ to Eq. (21) for $\mathfrak{K}/E = 100$ with η_B normalized so that $\eta_B(0) = 1$. The black and blue curves correspond to $\mathfrak{F}/\mathfrak{K} = 5$ and $\mathfrak{F}/\mathfrak{K} = 20$, respectively. As the wave force increases relative to the central force, ρ_s becomes broader and more wavelike.

that accounts for the local fluctuations of the pilot-wave. Using the fact that $|U_n| \ll 1$ (i.e., the distance between successive impacts is small relative to the Faraday wavelength), we approximate (13) and (14) by the continuous limit, in which the Gaussian noise is replaced by an increment of the Wiener process W_t over an infinitesimal timestep dt. This yields Langevin evolution equations for the position-velocity process (X_t, U_t) at time $t > 0$

$$dX_t = U_t \, dt, \tag{17}$$

$$dU_t = -\Big[D(U_t)U_t + \partial_x \mathcal{V}(X_t, t) \Big] dt + \sigma_0 \, dW_t, \tag{18}$$

where $\sigma_0 > 0$ prescribes the magnitude of the stochastic forcing. Here, we have defined the stochastic potential

$$\mathcal{V}(x, t) = \frac{1}{2} \mathfrak{K} x^2 + \mathfrak{F}\big(\eta_B * \rho\big)(x, t), \tag{19}$$

where $\rho(x, t)$ is the time-dependent probability distribution for the droplet's position.

The system (17) and (18) is speculative, and it should be noted that, unlike Theorem 1, the convolution $\big(\eta_B * \rho\big)(x, t)$ is for the time-dependent probability distribution and not for the stationary probability distribution. However, an initial condition $\rho(x, 0) = \delta(x)$ would correspond to prescribing the initial pilot-wave field as that of a bouncer, which is consistent with the numerical simulations of Sec. IV B. Moreover, if a stationary probability distribution $\rho_s(x)$ were to exist [where $\rho(x, t) \to \rho_s(x)$ as $t \to \infty$], then the system (17) and (18) would be consistent with the results of Theorem 1.

The evolution of the time-dependent joint probability distribution $p(x, u, t)$ corresponding to (17) and (18) is governed by the Vlasov-Fokker-Planck equation

$$\frac{\partial p}{\partial t} + u \frac{\partial p}{\partial x} = \frac{\partial}{\partial u} \Big\{ \big[\partial_x \mathcal{V}(x, t) + D(u)u \big] p \Big\} + \frac{\sigma_0^2}{2} \frac{\partial^2 p}{\partial u^2}, \tag{20}$$

where $\rho(x, t) = \int_\mathbb{R} p(x, u, t) \, du$ is the marginal distribution and $\mathcal{V}(x, t)$ is defined in Eq. (19). An interesting aspect of this equation is the nonlinearity and spatial nonlocality in $p(x, u, t)$ arising through $\mathcal{V}(x, t)$. Indeed, similar equations have been used in granular flow,[53] and it has been proved that such equations yield a unique stationary probability under suitable assumptions for the nonlinear drag D, the applied potential, and the convolution kernel η_B.[54,55] Self-propulsive particles

in the case of no spatial nonlocality ($\mathfrak{F} = 0$) have also been studied in a biological context.[56] The numerical solution to (20), with the possible inclusion of a velocity-dependent multiplicative noise $\sigma_0(u)$, will be the subject of future work.

While the case without self-propulsion $D(u) = D_0$ is not appropriate for modeling the dynamics of walking droplets, we note that the stationary distribution $\rho_s(x)$ to Eq. (20) satisfies Kramer's equation for a given potential $\mathcal{V}$, with implicit solution

$$\rho_s(x) = Z_0 \exp\left\{ -\frac{1}{E}\left[\frac{1}{2}\mathfrak{K}x^2 + \mathfrak{F}\big(\eta_B * \rho_s\big)(x) \right] \right\}, \tag{21}$$

where $E = \sigma_0^2/(2D_0)$ and Z_0 is a normalisation constant.[57] In Fig. 19, the numerical solution to (21) with different parameter values (solved using a Newton method) yields wave-like stationary statistics, a feature consistent with not only the pilot-wave dynamics of this system (Fig. 16) but also pilot-wave dynamics under a Coriolis force[23,27] and motion confined to a corral.[19,21] This provides a strong indication that the stochastic system (17) and (18) with the corresponding Vlasov-Fokker-Planck equation (20) will still exhibit wavelike statistics when the nonlinear drag $D(u)$ is included.

V. DISCUSSION

We have studied the dynamics of a droplet walking in a harmonic potential with its motion confined to a line. By performing linear stability analysis of the periodic states, we have captured the changes to the limit cycle dynamics as the wave force begins to dominate the harmonic potential. In particular, we have elucidated the oscillation amplitude quantization that appears at higher wave memory, which is analogous to the energy quantization in the quantum harmonic oscillator. We have also demonstrated that the pilot-wave has the lowest mean energy for stable oscillations, suggesting the significance of an underlying energy minimization principle in rationalising the quantized states.

The methods developed herein for analyzing periodic orbits are readily adaptable for studying the droplet motion in a harmonic potential without restricting the motion to a line, which will be useful for further characterization of the more exotic periodic orbital states observed in the laboratory (e.g., lemniscates and trefoils).[24,28] We expect some of these orbital states to be related by a (currently unknown) unstable branch in the parameter space, which is likely to connect two local minima of the wave's mean energy. Additionally, this methodology will allow for further analysis of the periodic motion observed between two droplets (in free-space), such as promenading pairs[15–17] and wobbling orbits.[13–15]

We have demonstrated that this system follows the Ruelle-Takens-Newhouse route to chaos, provided that the periodic state destabilizes via a pair of complex-conjugate eigenvalues. Furthermore, each of the new incommensurate frequencies that emerges after each of the first two bifurcations is approximated by the frequency of the corresponding unstable state, as predicted by the linear stability analysis. This result is a useful verification of our stability analysis and allows us to predict the dynamics of the quasi-periodic orbits.

Finally, we have uncovered the relationship between the mean wave field and the droplet statistics (Theorem 1), which represents a powerful diagnostic tool at extremely high wave memory. In this high memory regime, the droplet motion is reminiscent of a random walk, where the distance between successive turning points is prescribed by the minima of the local pilot-wave. By detrending the slow-timescale variations in the droplet's trajectory, we have highlighted the wave-like nature of the statistics, as becomes more pronounced at higher memory. We expect our approach to reveal the underlying statistical structure in other experimental configurations of this pilot-wave system, such as tunneling[8,10] and in corrals.[19,21]

Remarkably, the mean wave field yields an effective potential that has a controlling influence on the droplet dynamics and thus the emergent statistics. This draws further parallels to Bohmian mechanics, in which the statistical and guiding wave fields are identical.[58] Furthermore, we have proposed a Langevin equation to describe the dynamics in the high memory limit, where the motion is subject to an effective potential. By expressing the stationary probability distribution $\rho_s(x)$ as a (nonlinear) Vlasov-Fokker-Planck equation, we can solve directly for $\rho_s(x)$. We hope that these developments will lead to a fruitful comparison of the long-time behavior of this pilot-wave system in the chaotic regime to both statistical mechanics and Bohmian mechanics.

We expect the connection between the dynamics and statistics elucidated here to apply in other experimental configurations (such as corrals[19,21]) or indeed in a more generalized pilot-wave framework.[59] The generalization of Theorem 1 (as given by Appendix A) will play a key role in elucidating the link between the dynamics and statistics of pilot-wave systems and may provide a tool for better understanding the ingredients required for observing quantumlike behavior on a classical scale.

SUPPLEMENTARY MATERIAL

See supplementary material for videos of the periodic oscillatory pilot-wave dynamics.

APPENDIX A: STATISTICS IN A GENERALIZED PILOT-WAVE FRAMEWORK

In a generalized (linear) pilot-wave setting (with instantaneous impacts), the evolution of the fluid variables $\boldsymbol{u}(\boldsymbol{x}, t)$ may be written as $\boldsymbol{u}(\boldsymbol{x}, t_n^+) = \mathcal{L}\boldsymbol{u}(\boldsymbol{x}, t_{n-1}^+) + \boldsymbol{u}_I[\boldsymbol{x}, \boldsymbol{X}(t_n)]$, where $\boldsymbol{u}_I(\boldsymbol{x}, \boldsymbol{y})$ is the (not necessarily symmetric) pilot-wave field generated by a single impact at time $t = 0$ centred at $\boldsymbol{x} = \boldsymbol{y}$. The linear operator $\mathcal{L}$ maps the fluid variables from $t_{n-1}^+ \mapsto t_n^-$ with operator norm $||\mathcal{L}||_{op} < 1$ corresponding to a dissipative system. Assuming a stationary distribution $\mu(\boldsymbol{y})$ exists and that the dynamics are ergodic, then ergodicity gives $\bar{\boldsymbol{u}}(\boldsymbol{x}) = \mathcal{L}\bar{\boldsymbol{u}}(\boldsymbol{x}) + \int_{\mathbb{R}^2} \boldsymbol{u}_I(\boldsymbol{x}, \boldsymbol{y})\mu(\boldsymbol{y}) \, \mathrm{d}\boldsymbol{y}$, where $\bar{\boldsymbol{u}}(\boldsymbol{x}) \equiv \lim_{N\to\infty} \frac{1}{N} \sum_{n=1}^N \boldsymbol{u}(\boldsymbol{x}, t_n^+)$. Thus,

$$\bar{\boldsymbol{u}}(\boldsymbol{x}) = \int_{\mathbb{R}^2} \boldsymbol{u}_B(\boldsymbol{x}, \boldsymbol{y})\mu(\boldsymbol{y}) \, \mathrm{d}\boldsymbol{y},$$

where $\boldsymbol{u}_B(\boldsymbol{x}, \boldsymbol{y}) \equiv (\mathrm{Id} - \mathcal{L})^{-1}\boldsymbol{u}_I(\boldsymbol{x}, \boldsymbol{y})$ and Id is the identity operator. From the Neumann series $\sum_{n=0}^{\infty} \mathcal{L}^n = (\mathrm{Id} - \mathcal{L})^{-1}$, we recognize $\boldsymbol{u}_B(\boldsymbol{x}, \boldsymbol{y})$ as being proportional to the time-periodic Green's function for the domain centred at $\boldsymbol{x} = \boldsymbol{y}$, which is analogous to the wave field of a bouncer in a generalized framework.

APPENDIX B: ROBUSTNESS OF THE CONVOLUTION RESULT

To demonstrate the robustness of Corollary 1, we simulate the droplet motion in a parameter regime that corresponds to the stable periodic motion (see Sec. III) and compute the corresponding histogram $\mathcal{H}(x)$ to approximate the droplet's probability distribution $\rho_X(x)$ [Fig. 20(a)]. Thus, for histogram bin centres ξ_j with heights $\mathcal{H}(\xi_j)$, we have
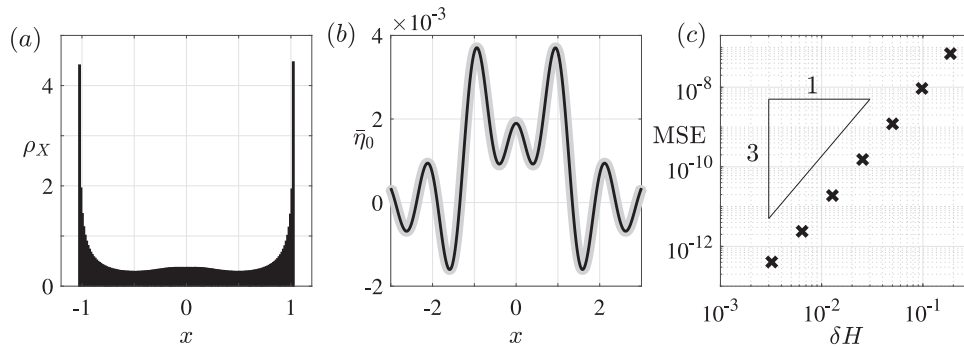

FIG. 20. Example convergence of Corollary 1 for periodic motion $X_n = X_{n+Q}$ in the case where $Q \to \infty$. (a) Histogram of the simulated periodic motion for $\Gamma/\Gamma_F = 0.95$ and $\tilde{\kappa} = 0.02$ over $N = 2 \times 10^5$ impacts. (b) Simulated mean wave field $\bar{\eta}_0^S(x)$ (gray) and computed mean wave field $\bar{\eta}_0^C(x)$ using the convolution (10) (black) for bin width $\delta H \approx 0.034$, where the histogram bin centres lie at $x = \xi_{\pm j} \equiv \pm j \, \delta H$ for $j \geq 0$. (c) Mean squared error MSE $\equiv N_X^{-1} \sum_{i=1}^{N_X} \left[\bar{\eta}_0^S(x_i) - \bar{\eta}_0^C(x_i) \right]^2$ for decreasing δH. The functions are evaluated at $N_X = 301$ equally spaced points x_i in the interval $[-3, 3]$. The slope indicates an $O(\delta H^3)$ convergence.

$\mathcal{H}(\xi_j) \approx \rho_X(\xi_j)$. For N_X equally spaced points x_i in the interval $[-3, 3]$, we compute the mean wave field $\bar{\eta}_0^C(x_i)$ using the convolution (10), with the midpoint quadrature rule $\bar{\eta}_0^C(x_i) \approx \delta H \sum_j \eta_B(x_i - \xi_j)\mathcal{H}(\xi_j)$. To compare the simulated mean wave field $\bar{\eta}_0^S$, we compute the mean squared error $\mathrm{MSE} \equiv N_X^{-1} \sum_{i=1}^{N_X} \left[\bar{\eta}_0^S(x_i) - \bar{\eta}_0^C(x_i)\right]^2$, which has size $O(\delta H^3)$ as $\delta H \to 0$ [Fig. 20(c)], thus indicating convergence.

APPENDIX C: ANALYSIS OF THE PERIODIC STATES

Following from Sec. III, we perform a Newton iteration to find the periodic states. Specifically, we solve $G(\theta) = 0$, where $\theta = (X_0, \tilde{\kappa}, G_1, \ldots, G_{N-1})$ and G (of dimension $N + 1$) is given below. The function G is dependent on several other functions of θ, which are computed at each step of the following algorithm. Hence, computation of the Jacobian $\partial G / \partial \theta^T$ requires an application of the chain rule, where the derivative $\partial / \partial \theta^T$ of each newly defined function is also computed. For an initial guess θ:

1. Use $\tilde{\kappa}$ and (5) to uniquely find $V_0^+(\theta)$ such that $X_1 - X_0 = 0$ (X_0 is an extremum).
2. Use the droplet iteration maps (5) and (7) with gradients G_n and the initial conditions $[X_0, V_0^+(\theta)]^T$ to compute positions $X_n(\theta)$ and velocities $V_n^-(\theta)$ for $n = 1, \ldots, N$.
3. For the wave field η_0 to satisfy the reflection conditions (12c) and (12d) with impacts $X_n(\theta)$, use (6) to find the initial wave amplitudes $a_m(t_0; k, \theta)$ and $a_m'(t_0^+; k, \theta)$, which solve

$$\left[(-1)^m I - M_k^N\right] \begin{pmatrix} a_m(t_0; k, \theta) \\ a_m'(t_0^+; k, \theta) \end{pmatrix} = -H_m(k; \theta) \begin{pmatrix} 0 \\ 1 \end{pmatrix},$$

where

$$H_m(k; \theta) = p_k \sum_{n=1}^{N} J_m[kX_n(\theta)]M_k^{N-n}.$$

4. Use (6) to recover the wave field $\eta_0(x, t_n; \theta)$ and gradients $g_n(\theta) = \partial_x \eta_0(X_n, t_n; \theta)$.
5. Using $g_N(\theta)$ and $V_N^-(\theta)$ with (7), compute $V_N^+(\theta)$.
6. For consistency with gradients and droplet reflection conditions (12a) and (12b), compute the output

$$G(\theta) = \begin{pmatrix} X_N(\theta) + X_0 \\ V_N^+(\theta) + V_0^+(\theta) \\ g_1(\theta) - G_1 \\ \vdots \\ g_{N-1}(\theta) - G_{N-1} \end{pmatrix}.$$

7. If $||G(\theta)||_\infty < \mathrm{TOL}$, stop. Otherwise, update θ with a Newton iteration and return to step 1.

To analyse the stability of the N-step periodic states, we extend the method used for the 1-step stability maps explored by Durey and Milewski,[15] where perturbations are now restricted to the x-axis. In brief, we linearize the map (5)–(7) about the periodic state at times t_n^+ for $n = 1, \ldots, N$. By expressing all the perturbed variables at time t_{n-1}^+ as a single column vector, we construct (sparse) transition matrices $T_n(\Gamma)$ to map the perturbed variables from $t_{n-1}^+ \mapsto t_n^+$ for $n = 1, \ldots, N$. The N-step stability matrix T is the product

$T = RT_N \cdots T_1$, where R is the diagonal reflection matrix about the x-axis. The eigenvalues of T are computed numerically, and the periodic state is defined to be asymptotically unstable if at least one eigenvalue lies outside the unit disc in the complex plane.

APPENDIX D: DETRENDING THE LONG-TIME STATISTICS

To detrend the data, we fit a simple version of a generalized additive model[60] to one of the aforementioned central bands of turning points. This yields a subset of turning point times $\mathcal{S} \subset \mathcal{T}$, which corresponds to the black data points in Fig. 15(a). This detrending technique is a form of regression, in which the trend curve $C(t)$ is expressed as a linear combination of smooth linearly independent basis functions (in this case, B-splines) whose weights are computed to give a least-squares fit of the data. However, to avoid over-fitting of the data [characterized by an excessively "wiggly" function $C(t)$], we introduce a smoothing penalization term.

As the trend changes over a timescale comparable to the memory time $M_e \gg 1$, we consider a linear combination of K basis functions $b_j(t)$, where KM_e is the simulation duration. The trend function $C(t)$ is thus given by the linear combination $C(t) = \sum_{j=1}^{K} \beta_j b_j(t)$, where β_j are the unknown coefficients. The penalty for over-fitting is chosen to minimize variation in the basis function coefficients β_j, where the required smoothness is determined by the parameter $\theta > 0$. The coefficients $\boldsymbol{\beta} = (\beta_1, \ldots, \beta_K)$ are then defined as the minimizer

$$\hat{\boldsymbol{\beta}} = \mathrm{argmin}_{\boldsymbol{\beta}} \sum_{i:\tau_i \in \mathcal{S}} \left[X(\tau_i) - C(\tau_i)\right]^2 + \theta S(\boldsymbol{\beta}),$$

with the smoothness penalization term

$$S(\boldsymbol{\beta}) = \sum_{j=2}^{K-1} (\beta_{j+1} - 2\beta_j + \beta_{j-1})^2.$$

Although methods exist to find the "optimal" value of θ for a given dataset,[60] it is sufficient for our purposes to simply fix $\theta = 500$ for all datasets considered, where the residual statistics vary only weakly for $100 \lesssim \theta \lesssim 1000$.

[1] J. Walker, "Drops of liquid can be made to float on the liquid. What enables them to do so?," Sci. Am. **238**, 151–158 (1978).
[2] Y. Couder, E. Fort, C.-H. Gautier, and A. Boudaoud, "From bouncing to floating: Noncoalescence of drops on a fluid bath," Phys. Rev. Lett. **94**, 177801 (2005).
[3] Y. Couder, S. Protière, E. Fort, and A. Boudaoud, "Walking and orbiting droplets," Nature **437**, 208 (2005).
[4] A. Eddi, E. Sultan, J. Moukhtar, E. Fort, M. Rossi, and Y. Couder, "Information stored in Faraday waves: The origin of a path memory," J. Fluid Mech. **674**, 433–463 (2011).
[5] L. de Broglie, *Ondes et mouvements* (Gautier Villars, 1926).
[6] Y. Couder and E. Fort, "Single-particle diffraction and interference at a macroscopic scale," Phys. Rev. Lett. **97**, 1541017 (2006).
[7] A. Eddi, J. Moukhtar, S. Perrard, E. Fort, and Y. Couder, "Level splitting at macroscopic scale," Phys. Rev. Lett. **108**, 264503 (2012).
[8] A. Nachbin, P. A. Milewski, and J. W. M. Bush, "Tunneling with a hydrodynamic pilot-wave model," Phys. Rev. Fluids **2**, 034801 (2017).
[9] G. Pucci, D. M. Harris, L. M. Faria, and J. W. M. Bush, "Walking droplets interacting with single and double slits," J. Fluid Mech. **835**, 1136–1156 (2017).

[10]A. Eddi, E. Fort, F. Moisy, and Y. Couder, "Unpredictable tunneling of a classical wave-particle association," Phys. Rev. Lett. **102**, 240401 (2009).

[11]S. Protière, Y. Couder, E. Fort, and A. Boudaoud, "The self-organization of capillary wave sources," J. Phys.: Condens. Matter **17**, 3529–3535 (2005).

[12]S. Protière, A. Boudaoud, and Y. Couder, "Particle-wave association on a fluid interface," J. Fluid Mech. **554**, 85–108 (2006).

[13]S. Protière, S. Bohn, and Y. Couder, "Exotic orbits of two interacting wave sources," Phys. Rev. E **78**, 036204 (2008).

[14]A. U. Oza, E. Siéfert, D. M. Harris, J. Moláček, and J. W. M. Bush, "Orbiting pairs of walking droplets: Dynamics and stability," Phys. Rev. Fluids **2**, 053601 (2017).

[15]M. Durey and P. A. Milewski, "Faraday wave-droplet dynamics: Discrete-time analysis," J. Fluid Mech. **821**, 296–329 (2017).

[16]J. Arbelaiz, A. U. Oza, and J. W. M. Bush, "Promenading pairs of walking droplets: Dynamics and stability," Phys. Rev. Fluids **3**, 013604 (2018).

[17]C. Borghesi, J. Moukhtar, M. Labousse, A. Eddi, E. Fort, and Y. Couder, "Interaction of two walkers: Wave-mediated energy and force," Phys. Rev. E **90**, 063017 (2014).

[18]B. Filoux, M. Hubert, and N. Vandewalle, "Strings of droplets propelled by coherent waves," Phys. Rev. E **92**, 041004(R) (2015).

[19]D. M. Harris, J. Moukhtar, E. Fort, Y. Couder, and J. W. M. Bush, "Wave-like statistics from pilot-wave dynamics in a circular corral," Phys. Rev. E **88**, 011001 (2013).

[20]T. Gilet, "Quantumlike statistics of deterministic wave-particle interactions in a circular cavity," Phys. Rev. E **93**, 042202 (2016).

[21]P. J. Sáenz, T. Cristea-Platon, and J. W. M. Bush, "Statistical projection effects in a hydrodynamic pilot-wave system," Nat. Phys. **14**, 315–319 (2018).

[22]E. Fort, A. Eddi, A. Boudaoud, J. Moukhtar, and Y. Couder, "Path-memory induced quantization of classical orbits," Proc. Natl. Acad. Sci. U.S.A. **107**(41), 17515–17520 (2010).

[23]D. M. Harris and J. W. M. Bush, "Droplets walking in a rotating frame: From quantized orbits to multimodal statistics," J. Fluid Mech. **739**, 444–464 (2014).

[24]S. Perrard, M. Labousse, M. Miskin, E. Fort, and Y. Couder, "Self-organization into quantized eigenstates of a classical wave-driven particle," Nat. Commun. **5**, 3219 (2014).

[25]A. U. Oza, D. M. Harris, R. R. Rosales, and J. W. M. Bush, "Pilot-wave dynamics in a rotating frame: On the emergence of orbital quantization," J. Fluid Mech. **744**, 404–429 (2014).

[26]M. Labousse, A. U. Oza, S. Perrard, and J. W. M. Bush, "Pilot-wave dynamics in a harmonic potential: Quantization and stability of circular orbits," Phys. Rev. E **93**, 033122 (2016).

[27]A. U. Oza, Ø. Wind-Willassen, D. M. Harris, R. R. Rosales, and J. W. M. Bush, "Pilot-wave hydrodynamics in a rotating frame: Exotic orbits," Phys. Fluids **26**, 082101 (2014).

[28]S. Perrard, M. Labousse, E. Fort, and Y. Couder, "Chaos driven by interfering memory," Phys. Rev. Lett. **113**, 104101 (2014).

[29]K. M. Kurianski, A. U. Oza, and J. W. M. Bush, "Simulations of pilot-wave dynamics in a simple harmonic potential," Phys. Rev. Fluids **2**, 113602 (2017).

[30]M. Labousse, S. Perrard, Y. Couder, and E. Fort, "Build-up of macroscopic eigenstates in a memory-based constrained system," New J. Phys. **16**, 113027 (2014).

[31]M. Labousse, "Etude d'une dynamique à mémoire de chemin: une expérimentation théorique," Ph.D. thesis (Université Pierre et Marie Curie-Paris VI, 2014).

[32]D. Ruelle and F. Takens, "On the nature of turbulence," Commun. Math. Phys. **20**, 167–192 (1971).

[33]S. Newhouse, D. Ruelle, and F. Takens, "Occurrence of strange axiom A attractors near quasi periodic flows on $t^m, m \geq 3$," Commun. Math. Phys. **64**, 35–40 (1978).

[34]Ø. Wind-Willassen, J. Moláček, D. M. Harris, and J. W. M. Bush, "Exotic states of bouncing and walking droplets," Phys. Fluids **25**, 082002 (2013).

[35]F. Dias, A. I. Dyachenko, and V. E. Zakharov, "Theory of weakly damped free-surface flows: A new formulation based on potential flow solutions," Phys. Lett. A **372**, 1297–1302 (2008).

[36]P. A. Milewski, C. A. Galeano-Rios, A. Nachbin, and J. W. M. Bush, "Faraday pilot-wave dynamics: Modelling and computation," J. Fluid Mech. **778**, 361–388 (2015).

[37]C. A. Galeano-Rios, P. A. Milewski, and J.-M. Vanden-Broeck, "Non-wetting impact of a sphere onto a bath and its application to bouncing droplets," J. Fluid Mech. **826**, 97–127 (2017).

[38]J. Moláček and J. W. M. Bush, "Drops walking on a vibrating bath: Towards a hydrodynamic pilot-wave theory," J. Fluid Mech. **727**, 612–647 (2013).

[39]J. Moláček and J. W. M. Bush, "Drops bouncing on a vibrating bath," J. Fluid Mech. **727**, 582–611 (2013).

[40]The computations were performed using Matlab 2016b, with a Core i5-4460 processor and 4GB of RAM.

[41]M. Abramowitz and I. Stegun, *Handbook of Mathematical Functions* (Dover Publications, 1964).

[42]A. U. Oza, R. R. Rosales, and J. W. M. Bush, "A trajectory equation for walking droplets: Hydrodynamic pilot-wave theory," J. Fluid Mech. **737**, 552–570 (2013).

[43]J. W. M. Bush, A. U. Oza, and J. Moláček, "The wave-induced added mass of walking droplets," J. Fluid Mech. **755**, R7 (2014).

[44]M. Labousse and S. Perrard, "Non-Hamiltonian features of a classical pilot-wave system," Phys. Rev. E **90**, 022913 (2014).

[45]M. Labousse, S. Perrard, Y. Couder, and E. Fort, "Self-attraction into spinning eigenstates of a mobile wave source by its emission back-reaction," Phys. Rev. E **94**, 042224 (2016).

[46]A. U. Oza, R. R. Rosales, and J. W. M. Bush, "Hydrodynamic spin states," Chaos **28**, 096106 (2018).

[47]S. Perrard, "A wave-mediated memory: Eigenstates, chaos and probabilities," Ph.D. thesis (Université Paris Diderot, 2014).

[48]L. D. Tambasco, D. M. Harris, A. U. Oza, R. R. Rosales, and J. W. M. Bush, "The onset of chaos in orbital pilot-wave dynamics," Chaos **26**, 103107 (2016).

[49]J.-P. Eckmann, "Roads to turbulence in dissipative dynamical systems," Rev. Mod. Phys. **53**, 643 (1981).

[50]T. Gilet, "Dynamics and statistics of wave-particle interactions in a confined geometry," Phys. Rev. E **90**, 052917 (2014).

[51]The functions $\mathfrak{F}$ and $\mathfrak{K}$ are easily expressed in terms of elementary functions, though their precise forms are omitted here for the sake of brevity.

[52]N. Sampara and T. Gilet, "Two-frequency forcing of droplet rebounds on a liquid bath," Phys. Rev. E **94**, 053112 (2016).

[53]S. McNamara and W. R. Young, "Kinetics of a one-dimensional granular medium in the quasielastic limit," Phys. Fluids A **5**(1), 34–45 (1993).

[54]F. Bouchut and J. Dolbeault, "On long time asymptotics of the Vlasov-Fokker-Planck equation and of the Vlasov-Poisson-Fokker-Planck system with Coulombic and Newtonian potentials," Differ. Integral Equ. **8**(3), 487–514 (1995), available at https://projecteuclid.org/euclid.die/1369316501.

[55]M. H. Duong and J. Tugaut, "Stationary solutions of the Vlasov-Fokker-Planck equation: Existence, characterization and phase-transition," Appl. Math. Lett. **52**, 38–45 (2016).

[56]U. Erdmann, W. Ebeling, L. Schimansky-Geier, and F. Schweitzer, "Brownian particles far from equilibrium," Eur. Phys. J. B **15**, 105–113 (2000).

[57]A. J. McKane, "Stochastic processes," in *Encyclopedia of Complexity and Systems Science*, edited by R. Meyers (Springer, New York, 2009), pp. 3097–3113.

[58]P. R. Holland, *The Quantum Theory of Motion: An Account of the de Broglie-Bohm Causal Interpretation of Quantum Mechanics* (Cambridge University Press, 2008).

[59]J. W. M. Bush, "Pilot-wave hydrodynamics," Annu. Rev. Fluid Mech. **47**, 269–292 (2015).

[60]S. N. Wood, *Generalized Additive Models: An Introduction with R* (Chapman & Hall/CRC, 2006).